Radiological Dose Calculations for the Diode Region of the Light Ion Fusion Target Development Facility

D.L. Henderson, M.E. Sawan and G.A. Moses

October 1986

UWFDM-707

Fus. Tech. 13 (May 1988) 594.

FUSION TECHNOLOGY INSTITUTE

UNIVERSITY OF WISCONSIN

MADISON WISCONSIN

Radiological Dose Calculations for the Diode Region of the Light Ion Fusion Target Development Facility

D.L. Henderson, M.E. Sawan and G.A. Moses

Fusion Technology Institute
University of Wisconsin
1500 Engineering Drive
Madison, WI 53706

http://fti.neep.wisc.edu

October 1986

UWFDM-707

Fus. Tech. 13 (May 1988) 594.

RADIOLOGICAL DOSE CALCULATIONS FOR THE DIODE REGION OF THE LIGHT ION FUSION TARGET DEVELOPMENT FACILITY

D.L. Henderson

M.E. Sawan

G.A. Moses

Fusion Technology Institute
1500 Johnson Drive
University of Wisconsin-Madison
Madison, Wisconsin 53706

October 1986

UWFDM-707

ABSTRACT

Biological dose rate calculations have been performed for a point external to the diode vacuum casing of the Target Development Facility for times following an operational period of 1 month. A new computational model has been developed for the radioactivity calculations to account for the sequential pulsed operation mode of the facility. The primary diode material considered is SS 304LN with an alternative material being aluminum 6061-T6. For the new pulse sequence model, it is shown that for both the stainless steel and aluminum diodes the dose rates external to the diode vacuum casing are above 1 rem/hr after a 1 day shutdown period. After a 1 week shutdown period, the dose rates have dropped to 90 and 12 mrem/hr, respectively.

1. INTRODUCTION

The Light Ion Beam Target Development Facility (TDF) is a proposed experimental facility intended to test small specially designed high gain ICF targets. During its peak operation period, the facility is to test ten to twelve 50-800 MJ fusion targets per day accumulating approximately 15,000 shots over a five year time period. Activation of the target, target chamber and surrounding components occurs as the high energy neutrons released by the initiation and subsequent burn of the DT fuel interact with the materials. Being an experimental device, the level of radioactivity induced by this number of high yield shots is of concern as access to the target chamber, the ion diodes and target diagnostic package may be required relatively soon after a shot or a number of shots. Thus it is of interest to examine viable low activation designs that minimize the induced radioactivity and biological doses in and near the target chamber.

The preliminary design of the TDF uses aluminum 6061-T6 as the chamber wall material and has the target explosion chamber submerged in a water pool as portrayed in Fig. 1. Previous steady state radioactivity and dose rate calculations for the bare Al-6061-T6 chamber wall and for the Au or W target debris accumulating onto the inner surface of the chamber wall have shown that the biological doses at the inner and outer surfaces of the wall are still quite significant, being 1.29 rem/hr at 1 week after shutdown, even with periodic removal of the target debris.[1] An examination of the nuclear decay products which lead to this high dose level shows that the decay products are mainly the result of neutron transmutation reactions above threshold energies in the range of 2-12 MeV. This in turn led to the placement of a 1 m thick, 40% porosity graphite moderating structure within the target chamber for the

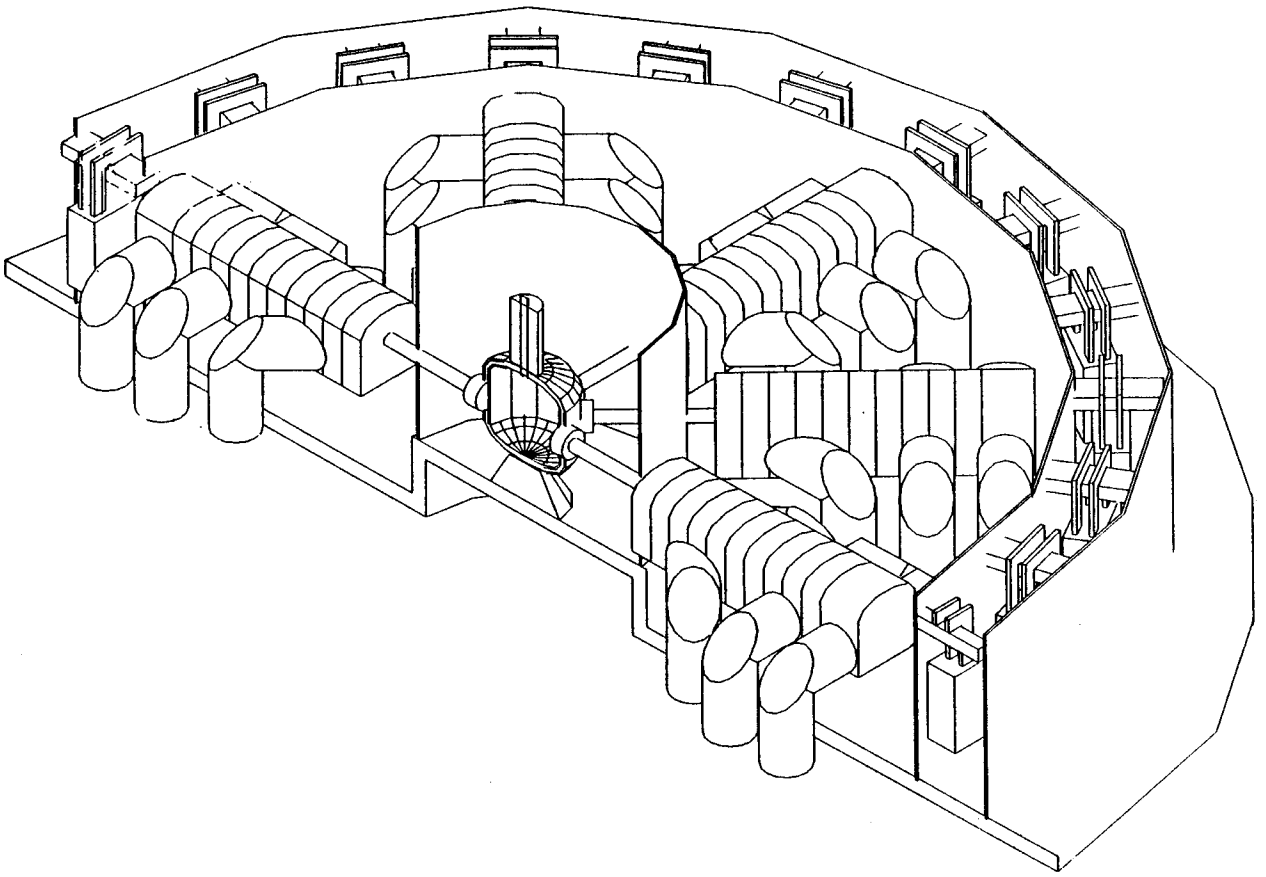

Fig. 1. Preliminary design of the Light Ion Fusion Target Development Facility.

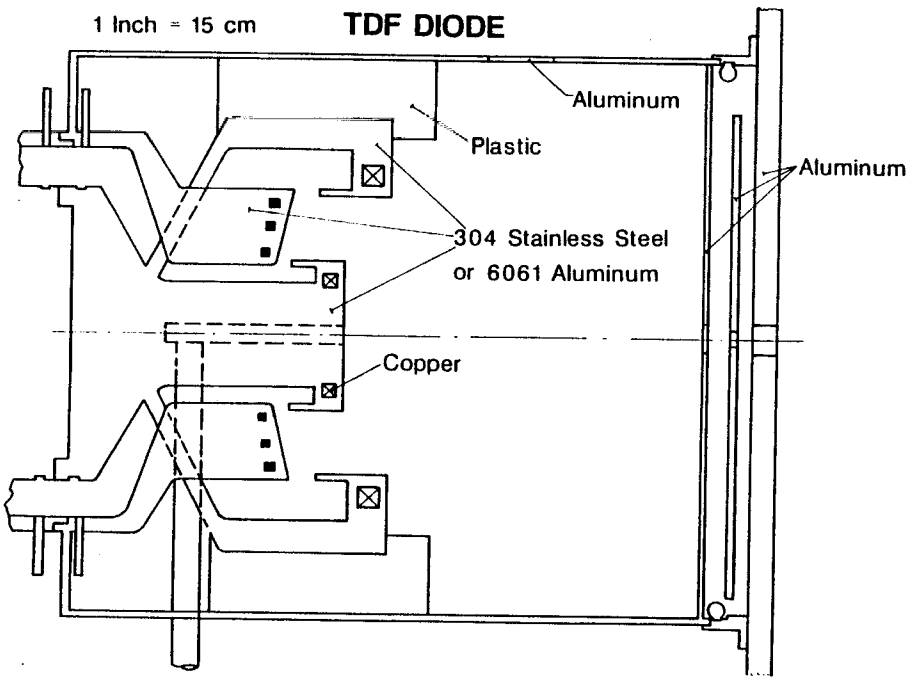

Fig. 2. Schematic of the high voltage ion diode used for the neutronic and dose rate calculations.

purpose of reducing the large component of high energy neutrons to below the neutron reaction threshold values prior to their interaction with the chamber.[2] The dose rate at the aluminum 6061-T6 target chamber outer surface was thus reduced from 1.29 rem/hr to 13.1 mrem/hr after a 1 week shutdown period.

One of the critical areas of the facility is the design of the high voltage diodes which convert the electrical pulse into ion beams. Depending on the repetition rate and lifetime of the diodes, the time allowable for maintenance and/or for exchange of the diode may be limited by the biological dose rate in the immediate vicinity of the ion diodes. Because of this need to know the dose rate, radioactivity and biological dose rate calculations have been performed for a point near the surface of the diode casing for the ion diode depicted in Fig. 2. Two ion diode materials are considered, the standard material being stainless steel 304LN and the alternative material being aluminum 6061-T6. Penetrations through the graphite moderator of 1 cm and 10 cm for plasma channels have also been considered. Dose rates computed by a newly developed computational model, which uses a more realistic pulse sequence scheme to account for the actual pulsed operation of the facility, are compared to the standard steady state assumption. These calculations represent an estimate of the biological dose near the vicinity of the ion diode.

A brief description of the data libraries and codes used in the neutronic and adjoint calculations is given in Section 2. Also contained therein are the calculational model and procedure for the computations and a discussion of the results. Section 3 contains a description of the data libraries and codes used in the radioactivity and dose rate calculations. This is followed by a

discussion of the newly developed pulse sequence model and the results. A summary of the results is given in Section 4.

2. NEUTRON TRANSPORT CALCULATIONS

2.1 Target Neutronics

The D-T fuel in ICF reactors is heated and compressed to extremely high densities (~ $10^{25}/cm^3$) before it ignites. A consistent neutronics analysis must, therefore, account for neutron target interactions which result in considerable spectrum softening of the fusion neutrons. This is done by performing neutron transport calculations for the compressed target configuration. The target design used in this analysis is an adaptation of a target design published by Bangerter and Meeker[3] and shown in Fig. 3. The target was modified by replacing the TaCOH ablator-pusher by a lithium-lead (Li-Pb) mixture that gives the same mass density, 1.26 g/cm^3.[4] The target DT load was assumed to be 1 mg and the fuel was assumed to be compressed to a density times radius product (ρR value) of 2 g/cm^2. The compressed target configuration used in the neutron transport calculations is shown in Fig. 4. The pusher is assumed to be compressed to the same mass density of the fuel with a ρR value of 1 g/cm^2. A tamper density that is 10% of the natural density was used to account for the effect of heating by the impinging ion beams.[5]

The multigroup one-dimensional discrete ordinates code ANISN[6] was used to perform the neutronics calculation for the target configuration at ignition. A combined RSIC DLC-41B/VITAMIN-C[7] and DLC-60/MACKLIB-IV[8] 25 neutron-21 gamma group cross section library was used in the calculation. An isotropic source of 14.1 MeV neutrons was distributed uniformly in the D-T fuel region. The calculated spectrum of neutrons escaping from the target,

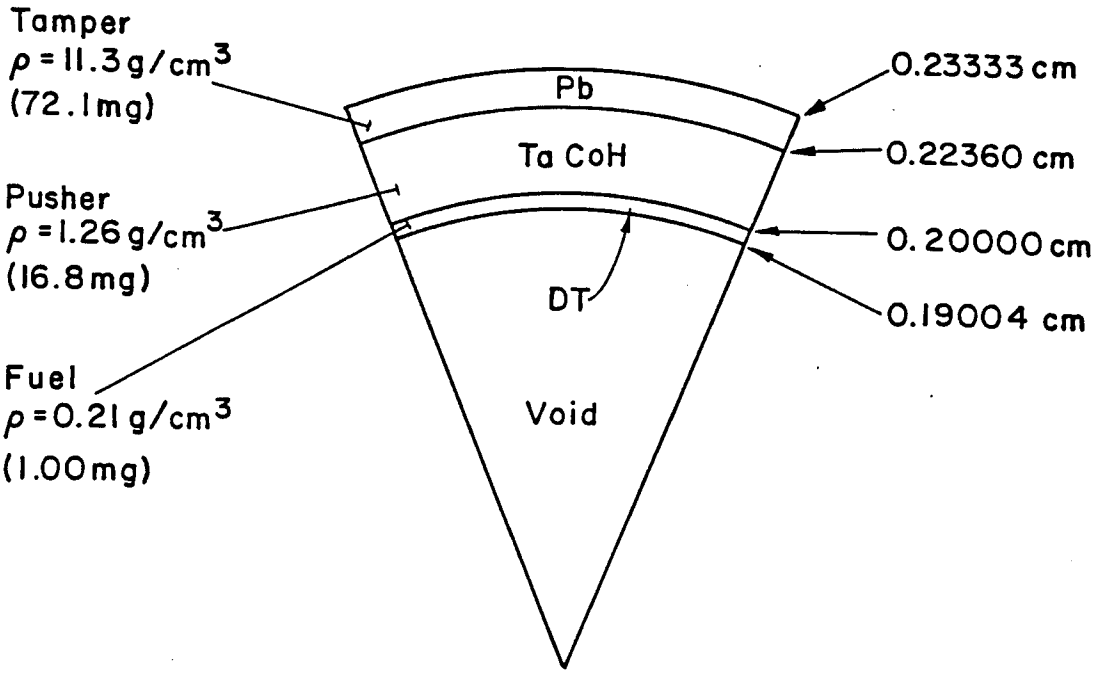

Fig. 3. Reference ion beam target as depicted in Ref. 3.

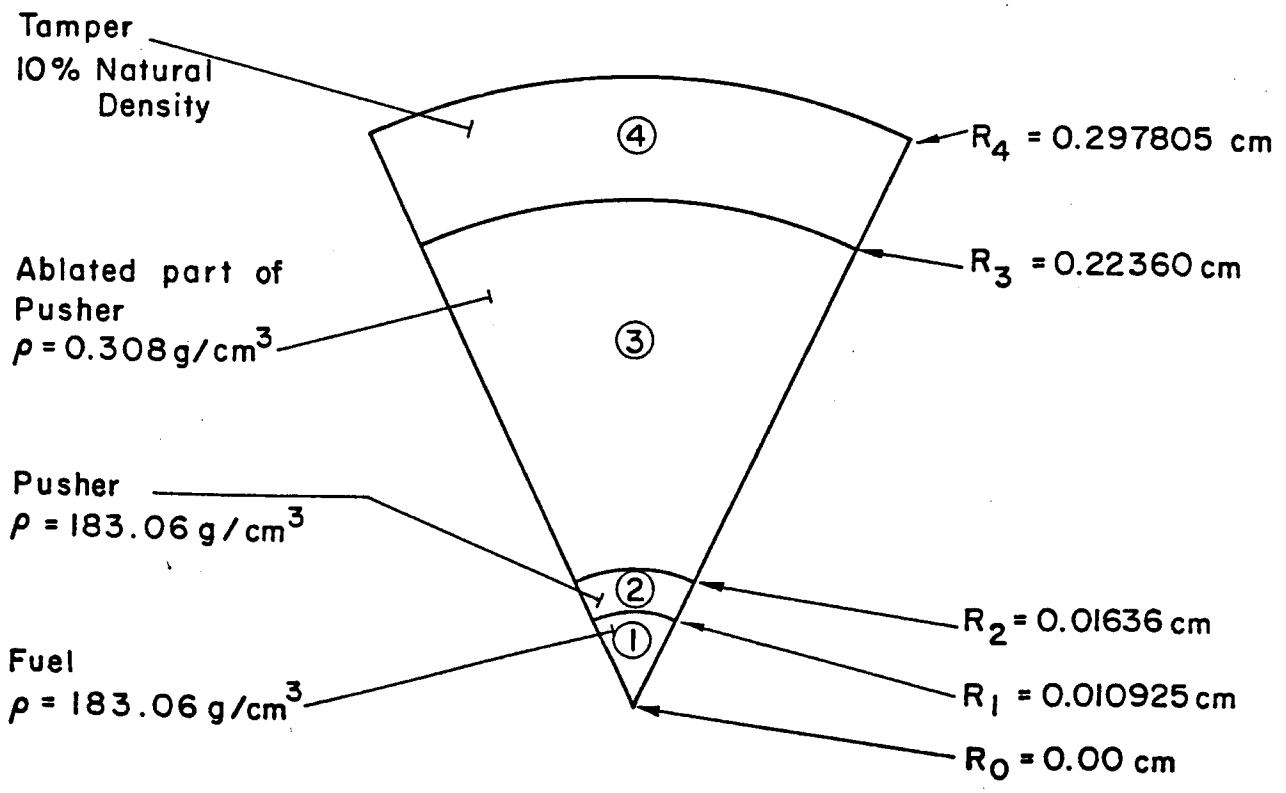

Fig. 4. The compressed target configuration used in the target neutronics calculations.

which represents the neutron source for the chamber calculation, is given in Fig. 5. The large peak at 14.1 MeV is due to the uncollided neutrons escaping from the target and amounts to 70.8% of leaking neutrons. Local peaking at 2 and 4 MeV is caused by backward elastic scattering of 14.1 MeV neutrons with deuterium and tritium. The low energy continuum spectrum consists of neutrons scattered elastically and inelastically within the target and of neutrons produced from (n,2n) and (n,3n) reactions. The average energy of the neutrons emanating from the target is 12 MeV. The results indicate that for each D-T fusion, 1.046 neutrons leak from the target mainly due to (n,2n) reactions in the dense D-T fuel. This implies that ~ 71% of the target yield is carried by neutrons. A fuel burnup fraction of 30% was assumed giving approximately 100 MJ of fusion energy released from the 1 mg fuel target used in the calculations. Since the TDF target is required to produce a yield of 200 MJ a D-T mass of 2 mg will be needed. For the same ignition ρR value, intrinsic quantities such as neutron spectrum are assumed not to change while absolute quantities such as neutron yield are scaled by a factor of 2. A 200 MJ target D-T yield corresponds to 7.09×10^{19} D-T fusions per shot and 7.42×10^{19} neutrons emanating from the target per shot. The neutron spectrum obtained from the target neutronics calculation was used to represent the source for the chamber neutronics.

2.2 One-Dimensional Calculational Model for the Target Chamber

The cylindrically shaped target chamber is approximated by spherical geometry for the one-dimensional calculations. The results, therefore, represent the conditions at the facility midplane. A schematic of the TDF target chamber model used in the one-dimensional calculation is given in Fig. 6. The 1 cm thick graphite liner is located at a radius of 2 m and is followed by a

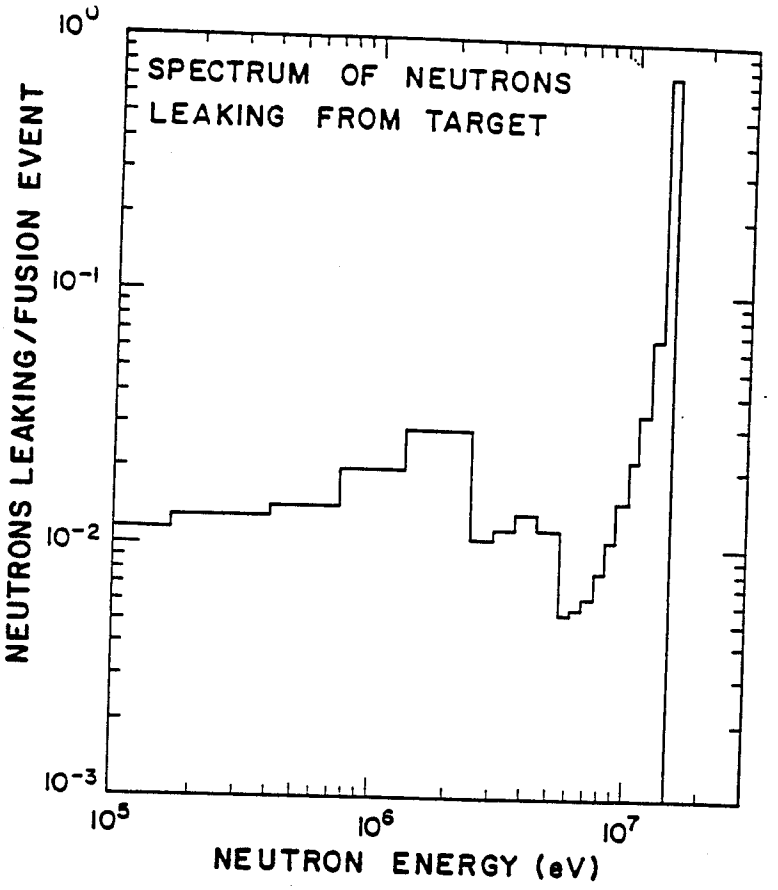

Fig. 5. Spectrum of neutrons emerging from the target.

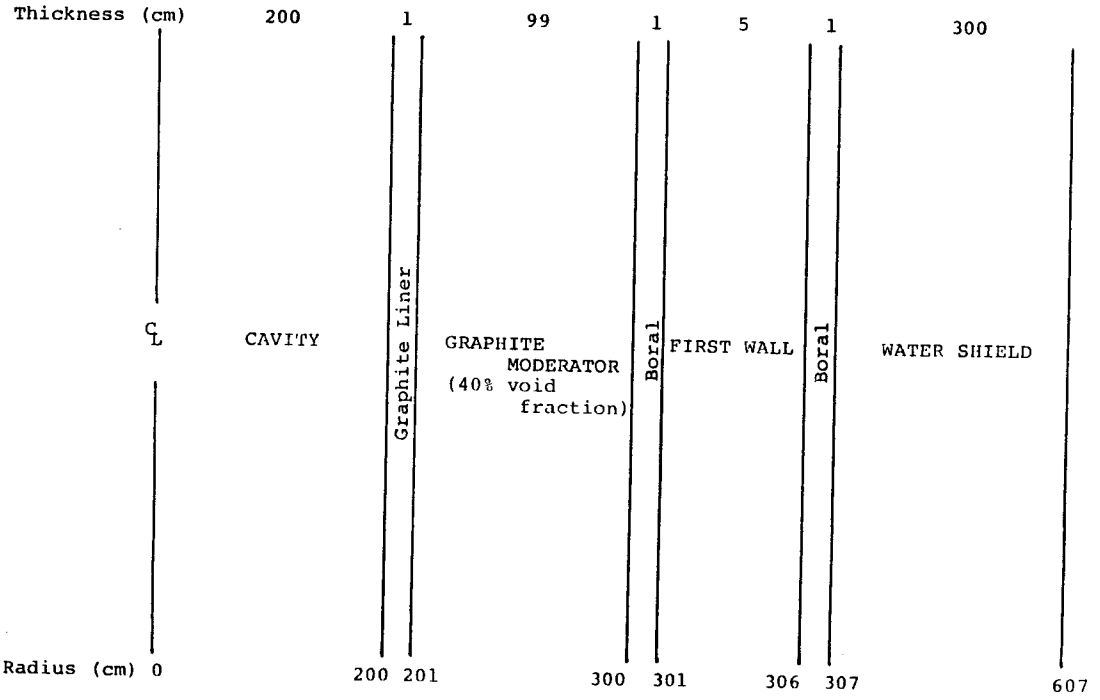

Fig. 6. Schematic of the TDF chamber used in the one-dimensional neutronics calculation.

99 cm thick graphite moderator having a 40% void fraction. The 5 cm thick aluminum 6061-T6 first wall is surrounded by two 1 cm thick layers of Boral. A 3 m thick water shield is used around the target chamber. Appendix A gives the composition for the materials used in the calculations. The source is considered to be a point isotropic source at the center of the cavity. The neutron and gamma spectra obtained from the target neutronics calculation were used to represent the source for the chamber calculation. The calculations, therefore, account for neutron spectrum softening, neutron multiplication, and gamma production in the target. The one-dimensional discrete ordinates code ONEDANT[9] was used together with the LANL MATXS5[10] cross section data library processed from the ENDF/B-V[11] evaluated files using the NJOY[12] code. The standard LANL 30 neutron-12 gamma group structure was used. The calculations were performed using the P_3-S_8 approximation. The calculation uses 20 seconds of Cray-XMP time.

The primary objective of the neutronics analysis for TDF is to determine the neutron flux in the different facility components which represents the source for the activation calculations. The one-dimensional target cavity calculation discussed above is used as the first step in the calculation of the flux distribution in the diode. The energy and angular distribution of neutrons and gamma photons incident on the graphite liner are calculated and used to represent a surface source in the second step of the calculation where the detailed geometrical configuration of the diode is modeled. Since the beam ports occupy only 0.5% of the liner inner surface area, the one-dimensional calculation in which the penetrations are not modeled gives a fairly accurate estimate of the nuclear radiation incident on the surface of the liner and the beam penetration opening. In addition, since the diodes are

located in the facility midplane, using spherical geometry in the one-dimensional calculation yields reasonably accurate results for nuclear radiation incident on the area around the beam ports.

2.3 Nuclear Radiation Incident on the Liner

The energy spectra of neutrons and gamma photons incident on the inner surface of the graphite liner are shown in Figs. 7 and 8. The results represent the integral over all directions going into the liner and are normalized to one D-T fusion and are given per energy group of the 30 neutron-12 gamma standard LANL group structure. Included also for comparison are the spectra of neutrons and gamma photons emerging from the target. For each D-T fusion in the target, 1.046 neutrons emanate from the target and impinge directly on the liner. Neutron scattering collisions in the graphite moderator result in reflecting some of these neutrons back into the cavity. These reflected neutrons will end up impinging on the liner with a fraction of them reflected again into the cavity. Our results indicate that for each D-T fusion, 5.712 neutrons end up reentering the cavity and a total of 6.758 neutrons will be incident on the liner. The neutrons coming directly from the target represent only 15% of the total impinging neutrons which explains the much softer neutron energy spectrum compared to that emerging from the target. Together with the reflection of gamma photons by the material surrounding the cavity, gamma generation in the surrounding material enhances the number of photons reentering the cavity. The gamma photons coming directly from the target represent only 3% of the 0.541 total number of photons incident on the liner per D-T fusion.

The angular distribution of neutrons and gamma photons incident on the liner are given in Fig. 9. The results are normalized to 1 D-T fusion and

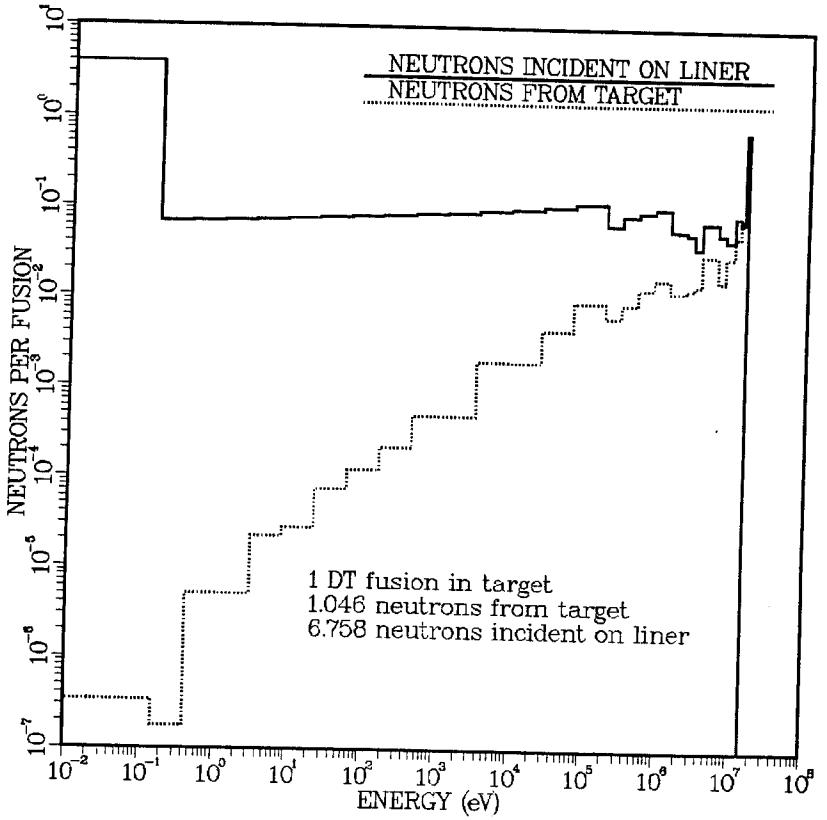

Fig. 7. Energy spectrum of neutrons incident on the graphite liner.

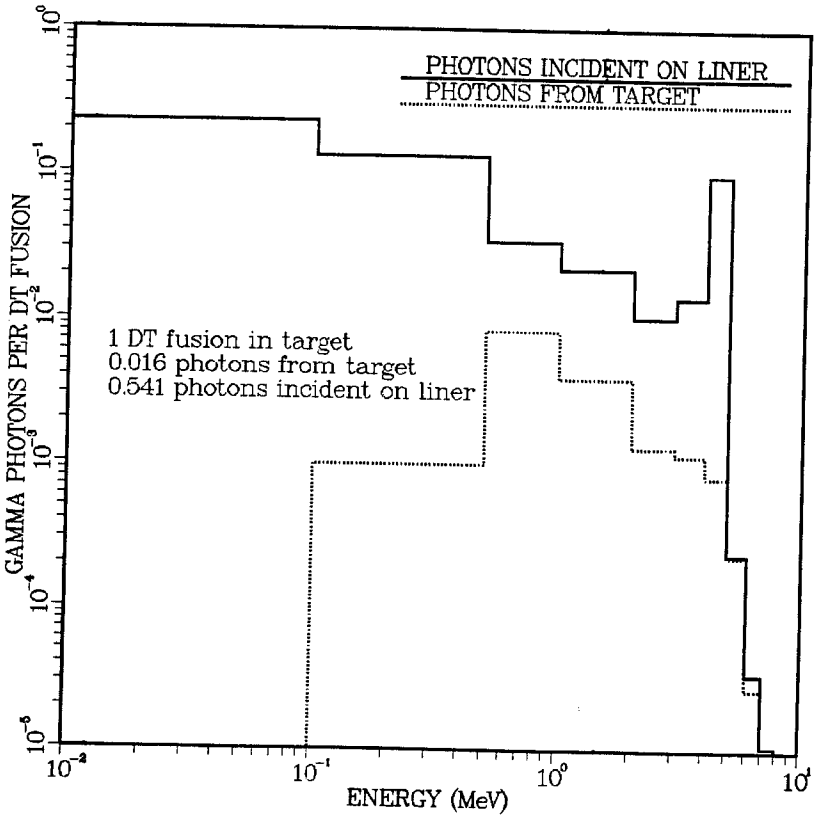

Fig. 8. Energy spectrum of gamma photons incident on the graphite liner.

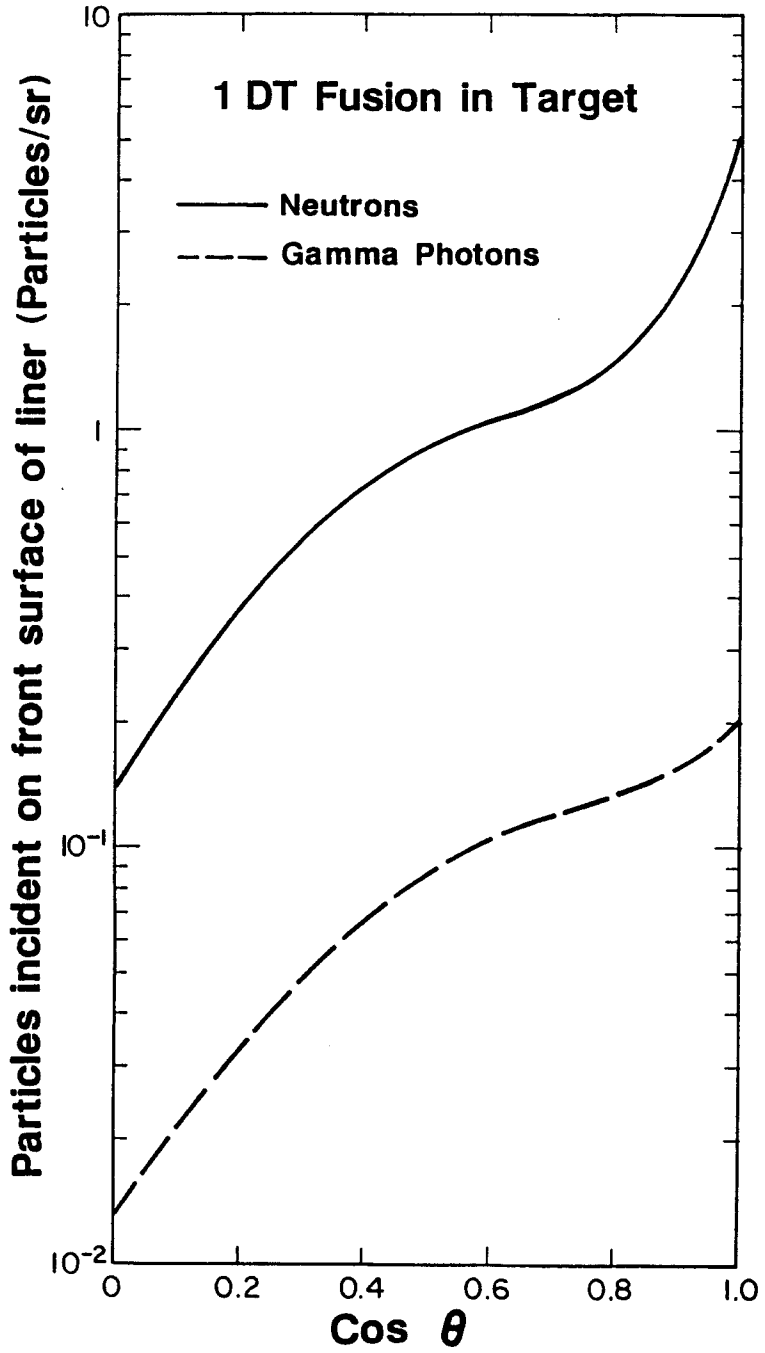

Fig. 9. Angular distribution of neutrons and gamma photons incident on the liner.

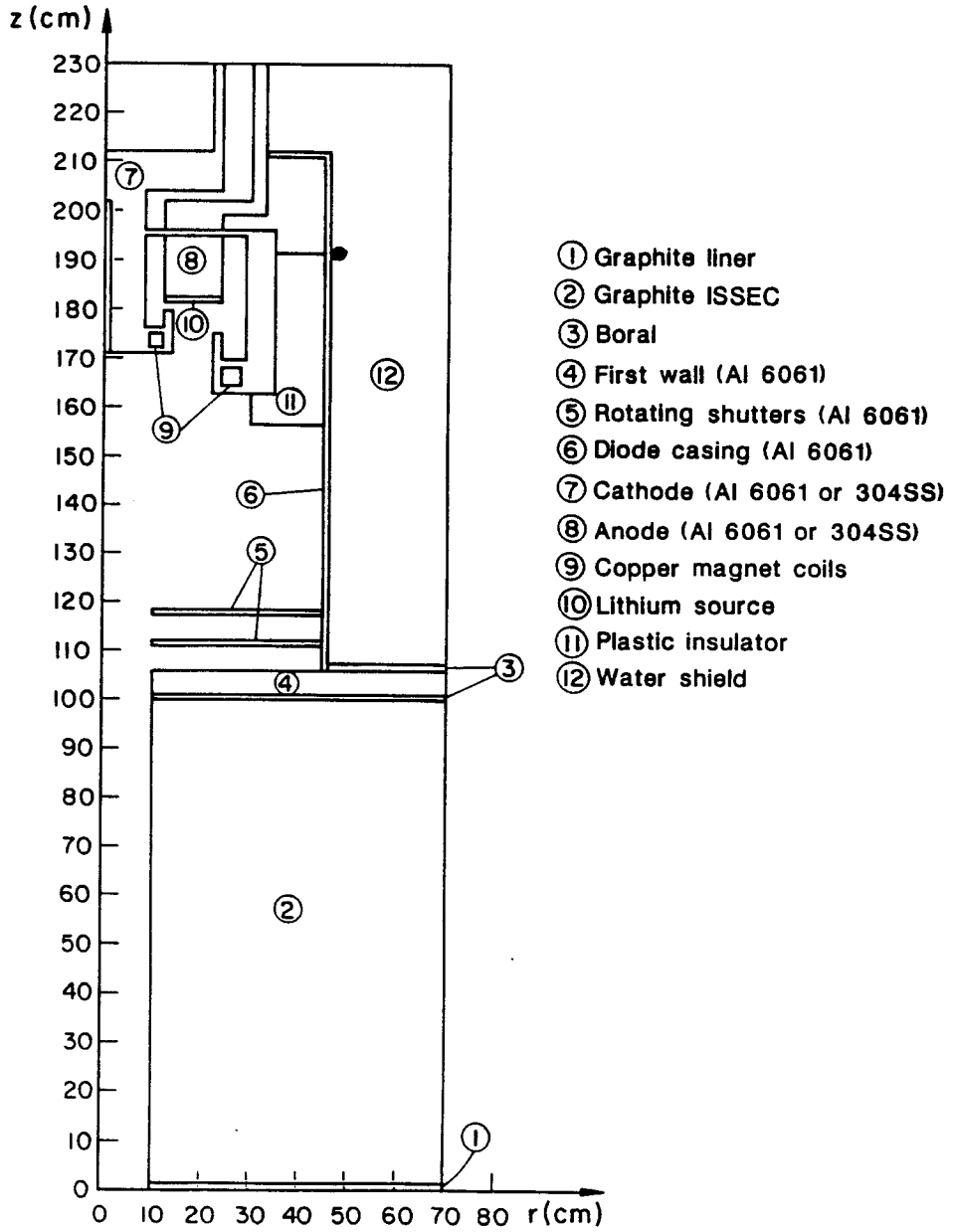

Fig. 10. The r-z geometrical model used in the two-dimensional neutronics and activation calculations.

represent values integrated over all energies. The angle θ is measured from the normal to the surface. It is clear that the angular distribution peaks at normal incidence. The peaking is less pronounced for gamma photons due to the smaller direct contribution from the target. It should be pointed out that the angular distribution of incident neutrons varies from one energy group to the other. Peaking in the normal direction is more pronounced for high energy groups where the direct contribution from the target is large. The energy spectra of neutrons and gamma photons incident on the liner in the discrete ordinates directions are stored to serve as surface source distributions in the two-dimensional calculation that properly models the detailed diode geometry.

2.4 Two-Dimensional Calculational Model for the Diode

Two-dimensional neutronics calculations have been performed to determine the flux distribution in the diode. The diode geometry was modeled in two-dimensional r-z geometry. The geometrical model shown in Fig. 10 is an idealization and adaptation of the actual diode design. Appendix A gives the composition of the materials used in the different zones. Calculations have been performed for two penetration radii of 10 and 1 cm. The option of using aluminum 6061-T6 for the cathode and anode instead of stainless steel 304LN was also considered. Hence, four two-dimensional neutronics calculations have been performed with the different penetration radii and diode materials.

The two-dimensional discrete ordinates code TWODANT[13] was used in the calculations with the same 30 neutron-12 gamma multigroup cross section data based on the ENDF/B-V evaluation which was used in the one-dimensional calculation. A spatially uniform surface source was used at the bottom boundary represented by the energy dependent angular flux at the inner surface of the

liner as obtained from the one-dimensional calculation. The source is given in the four discrete ordinates directions going into the graphite moderator. The source is assumed to be uniform in the azimuthal direction. A vacuum boundary condition is used at the bottom boundary since the contribution from neutrons reentering the cavity from the moderator is already taken into account in the surface source. A right reflecting boundary is used at a radius of 70 cm which is roughly half the distance between the centerlines of adjacent diodes. A vacuum boundary is used at the top. 32 radial and 77 axial fine mesh intervals were used leading to flux calculations at 2464 mesh points. Each calculation took 2 min of Cray-XMP CPU time.

In addition to the forward neutron transport calculations, adjoint gamma transport calculations were performed for the four cases considered here. In the adjoint calculations, an adjoint source was used on the outer surface of the diode casing at z = 190 cm with the energy spectrum given by the gamma flux-to-dose conversion factors. These calculations were used to determine the adjoint dose field distribution that is coupled with the decay gamma source to yield the dose at this position for various times after shutdown.

The two-dimensional calculational model used here has several shortcomings that introduce uncertainties in the results. In order to model the detailed three-dimensional geometry for the deterministic two-dimensional discrete ordinates calculation several adaptations were made to yield the idealized geometrical model shown in Fig. 10. Furthermore, the actual planes of symmetry cannot be included in the two-dimensional geometrical model necessitating the use of a cylindrical reflecting boundary to account for the contribution from the surrounding regions. Since the diodes are located on the facility midplane, each diode is surrounded by two diodes on opposite sides.

Even though the cylindrical reflecting boundary is located at half the distance between the centerlines of the two adjacent diodes, its use is equivalent to surrounding the modeled diode by diode penetrations at all azimuthal locations. This tends to overestimate the flux and dose in the diode area. Another geometrical problem stems from using a planar disc source at the bottom boundary of the r-z model. The model does not take into account the geometrical attenuation of the flux which can be significant particularly for the component coming directly from the target at the center of the cavity. The $1/R^2$ geometrical attenuation implies a geometrical attenuation factor of ~ 3 for the flux as one goes from the front of the graphite moderator to the front of the diode. It is clear, therefore, that the geometrical approximations introduced by the two-dimensional model tend to overestimate the flux and dose in the diode region. The only way to avoid these geometrical modeling deficiencies is to use the Monte Carlo method where the detailed three-dimensional geometry can be modeled. However, the Monte Carlo method is statistical in nature and is not capable of generating accurate estimates for differential quantities such as the neutron energy spectra in optically thin zones which are required for activation and dose calculations. Several tens of CRAY hours might be needed to produce the energy and spatial distribution of the neutron flux to the same level of detail as obtained from the deterministic two-dimensional discrete ordinates calculational procedure used in this work.

Another shortcoming of the model used here is an inherent problem in the discrete ordinates method referred to as the ray effect. It is related to the fact that the angular flux is given only in certain discrete directions. It is, therefore, not possible to exactly represent the component in the normal

direction (μ = 1). 15% of the neutrons incident on the penetration opening come directly from the target in the normal direction. However, these neutrons are assumed to be in the direction μ = 0.962 (θ = 15.8°) and will end up impinging on the penetration wall rather than streaming directly to the diode. Since the contribution of the primary neutrons from the target decreases considerably for lower energy neutrons as shown from Fig. 7, the underestimation of the flux in the diode is more pronounced for high energy neutrons. Our calculations indicate that for the 14 MeV neutrons an order of magnitude attenuation occurs in the 1 m long penetration while two orders of magnitude attenuation occurs in the graphite moderator. If no attenuation takes place in the penetration, as should be expected in the actual case, we estimated that a factor of ~ 2.5 more 14 MeV neutrons will be entering the diode region. To quantify this effect we performed a calculation for the case of the steel diode and 10 cm radius penetration with the thickness of the moderator reduced to 30 cm and its density increased to preserve the optical thickness. In this calculation neutrons incident on the duct opening in the direction μ = 0.962 are forced to stream into the diode. This tends to overestimate the flux in the diode for low energy neutrons where the contribution coming directly from the target is small. In addition, the streaming neutrons are forced to impinge on the outer part of the diode leading to higher dose levels outside the diode casing. The results of this calculation will be used to indicate an upper bound for the biological dose level.

The Monte Carlo method eliminates the ray effect problem but is expensive with significant statistical uncertainties in results. An alternate approach is to evaluate the first collision source[14] which can then be used as a volumetric source in the discrete ordinates calculation. In this case, the

contribution from the secondary neutrons reentering the cavity should be considered separately and added to the contribution from the primary target neutrons which are treated using the first collision source method. It should be emphasized that this approach does not eliminate the geometrical modeling problems discussed above.

The two-dimensional calculational procedure used here is considered to be good enough in this preliminary stage of the design due to the expected counterbalancing geometrical and ray effects discussed above. When detailed diode and chamber designs become available we plan to perform the calculations using the Monte Carlo method or the first collision source to circumvent the shortcomings of the calculational model used here.

2.5 Neutron Flux in the Diode

The neutron energy spectrum was determined at the 2464 mesh points used in the two-dimensional model. This neutron flux distribution was used as the source for the activation calculations. Figure 11 shows the energy spectra of neutrons leaking from the back of the diode for three of the cases considered. The results are normalized to 1 D-T fusion and are given per energy group. The streaming neutrons have a softer spectrum in the case of the aluminum diode than in the case of the steel diode. The streaming neutrons at the back of the diode are a factor of ~ 3.5 higher for the aluminum diode than for the steel diode. This indicates that more neutrons are attenuated in the steel diode that could lead to more activation. The results of Fig. 11 indicate that the energy spectrum at the back of the diode is not affected by the penetration size while the total number of neutrons is reduced by a factor of ~ 2.4 as the penetration radius goes down from 10 to 1 cm.

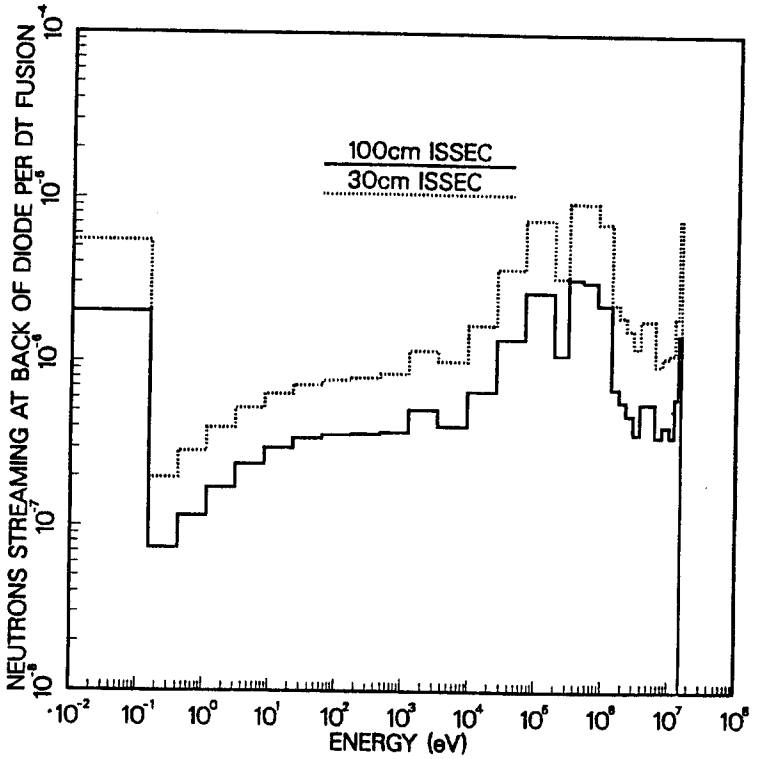

Fig. 11. Energy spectra of neutrons streaming at the back of the diode for different diode materials and penetration sizes.

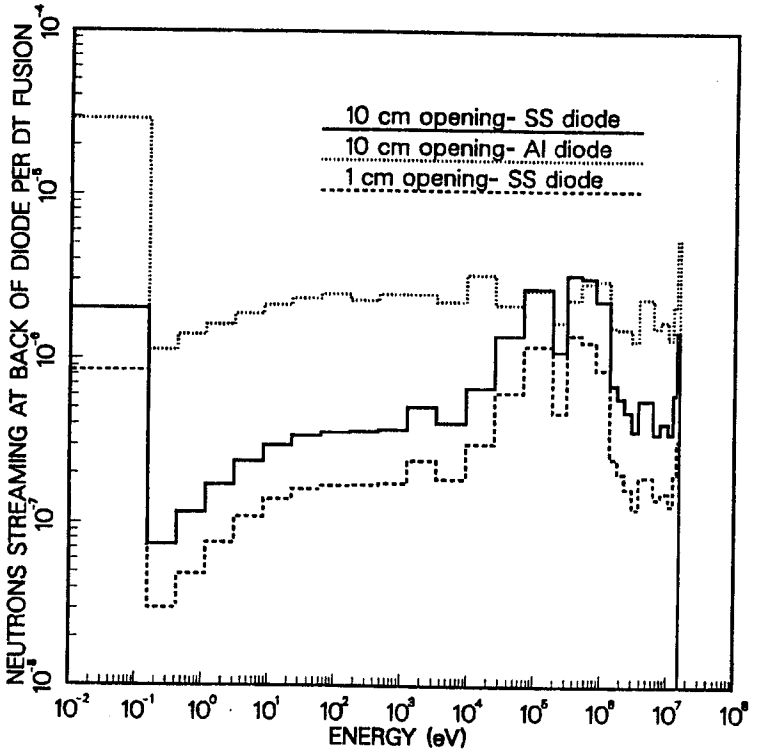

Fig. 12. Energy spectrum of neutrons streaming at the back of the steel diode with 10 cm radius penetration compared to the case with reduced graphite moderator thickness to force neutrons in the direction $\mu = 0.962$ to stream to the diode.

As pointed out in the previous section the calculations are expected to underestimate the streaming of neutrons into the diode due to the ray effect problem. The calculation performed with neutrons incident on the penetration opening in the direction $\mu = 0.962$ forced to stream all the way to the diode indicated that for a 10 cm penetration opening and steel diode the number of neutrons at the back of the diode is enhanced by a factor of ~ 3 with a slightly harder spectrum as shown in Fig. 12. A much lower enhancement is expected for the 1 cm penetration radius case. This implies that the number of neutrons streaming at the back of the diode could increase by a factor of ~ 6 when the penetration radius is increased from 1 to 10 cm.

Figures 13-16 show the radial distribution of the neutron flux in energy groups 2 (13.5-15.0 MeV), 7 (3.68-6.07 MeV), 20 (1.235-3.35 keV), and 30 (thermal group), respectively for the 10 cm penetration radius and steel diode. The results are normalized to 1 D-T fusion/s and are shown for three axial locations: back of graphite moderator ($z = 100$ cm), front of diode ($z = 170$ cm), and back of diode ($z = 210$ cm). The results given by dashed lines represent the case where neutrons incident on the penetration opening in the direction $\mu = 0.962$ are forced to stream into the diode by using a 30 cm thick moderator. It is clear that about an order magnitude higher 14 MeV flux is obtained at the back of the 100 cm long penetration in the 30 cm thick graphite moderator case. The effect is less pronounced for the lower energy groups. The 14 MeV flux at the front of the diode has a pronounced off-axis peak at $r \simeq 20$ cm which is related to the discrete directions used. The peak is more pronounced for the 30 cm thick moderator since neutrons in the direction $\mu = 0.962$ stream directly to the diode without being attenuated in the moderator as is the case for the 100 cm thick graphite moderator. This indi-

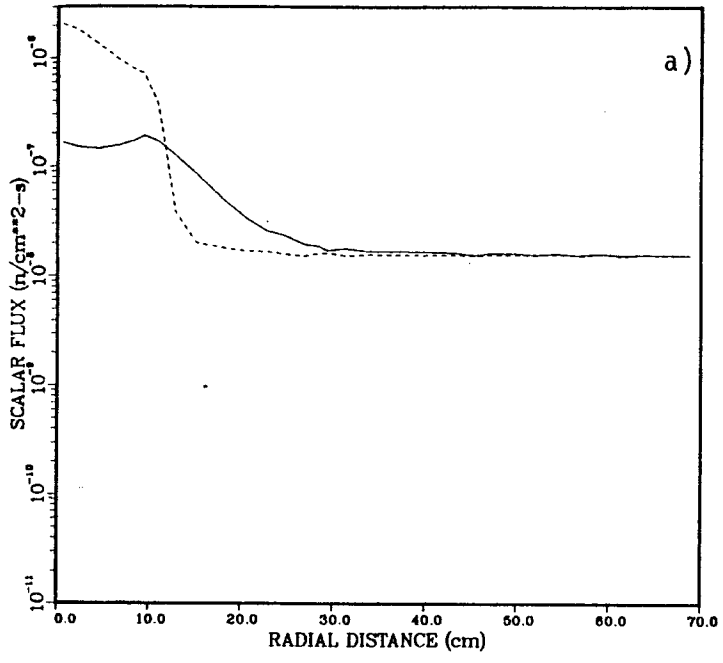

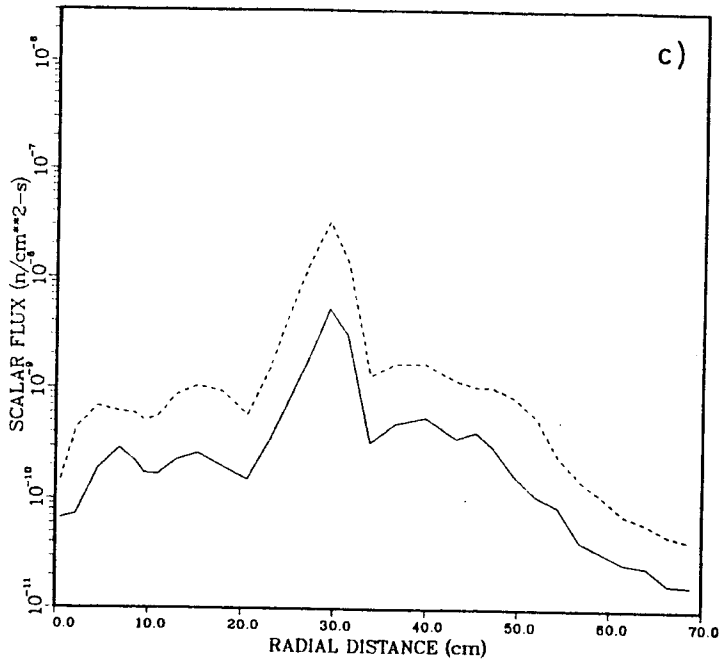

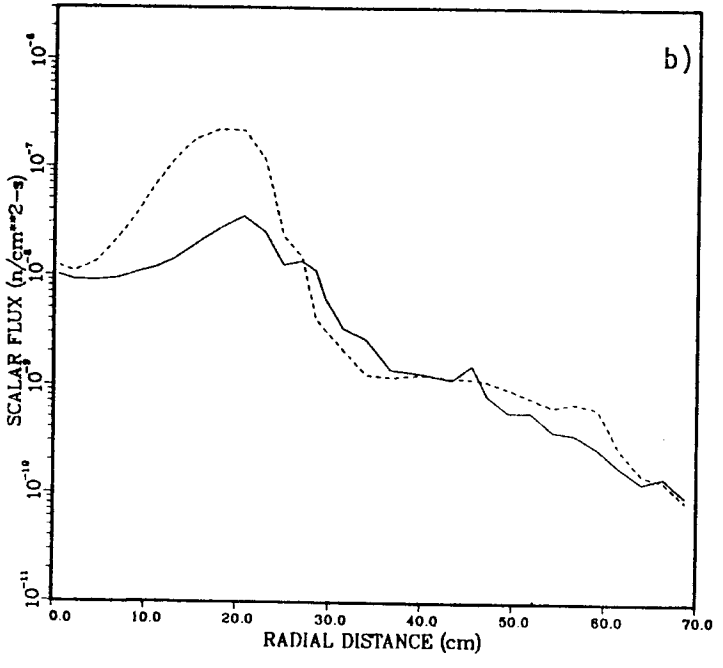

Fig. 13. Radial distribution of the neutron flux in group 2 for three axial positions; a) lack of graphite moderator (z = 100 cm), b) front of diode (z = 170 cm) and c) back of diode (z = 210 cm).

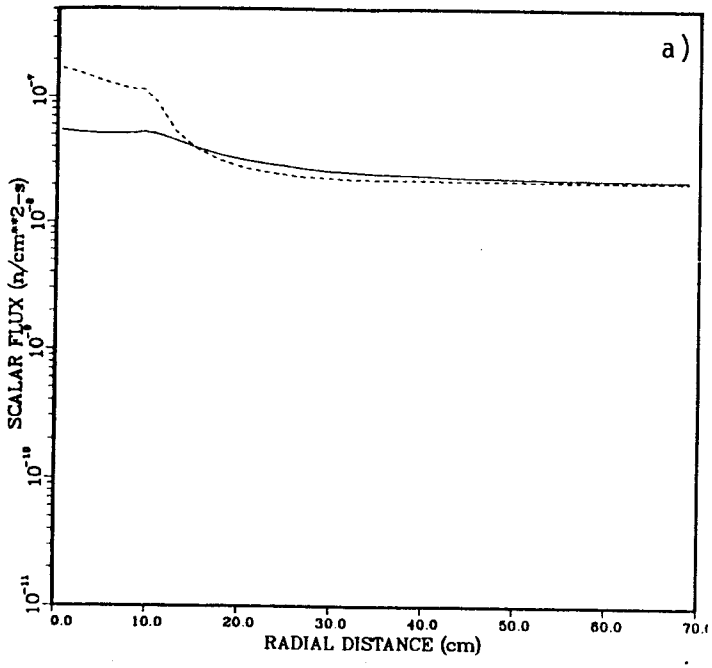

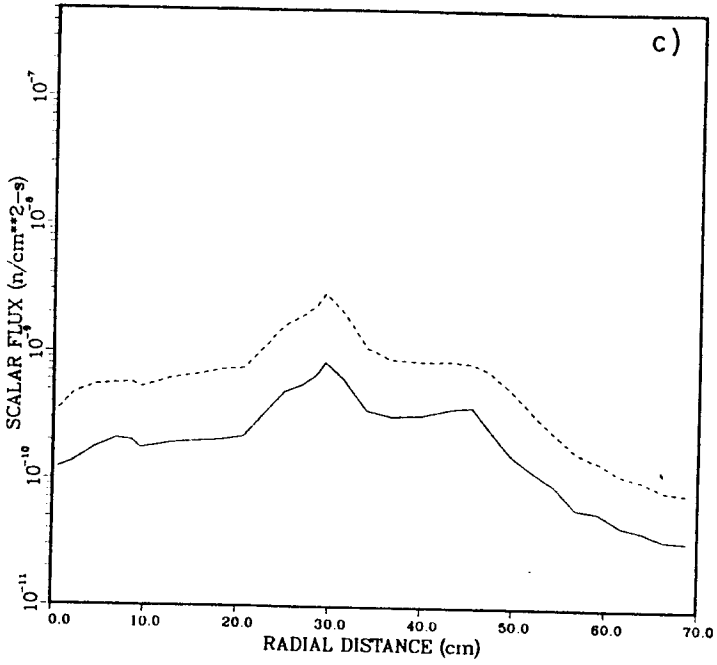

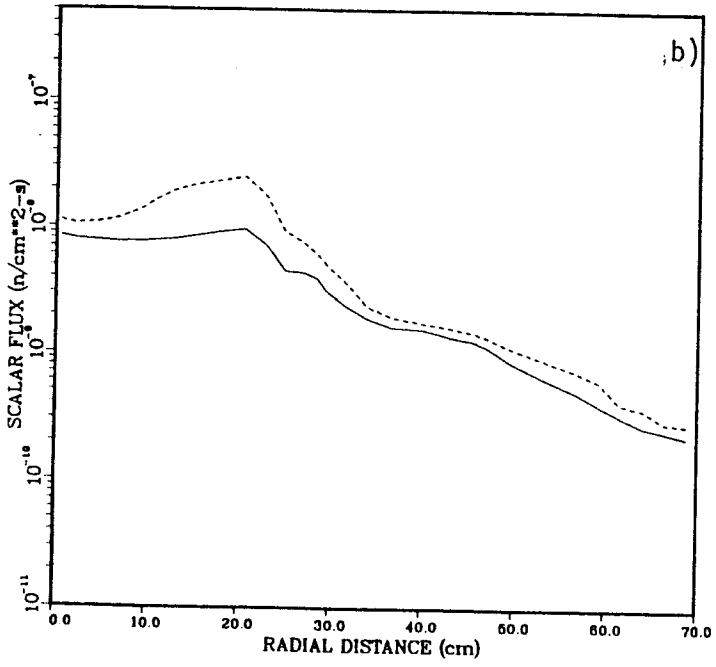

Fig. 14. Radial distribution of the neutron flux in group 7 for three axial positions; a) back of graphite moderator (z = 100 cm), b) front of diode (z = 170 cm), and c) back of diode (z = 210 cm).

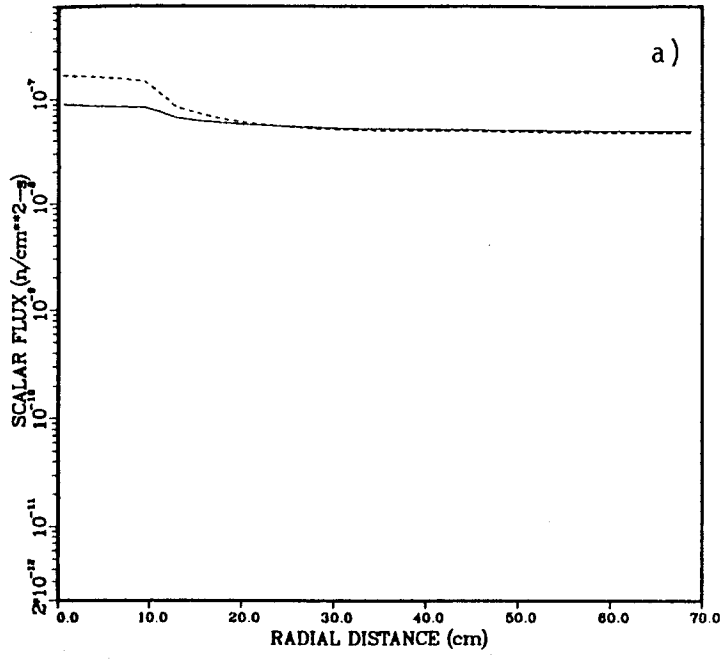

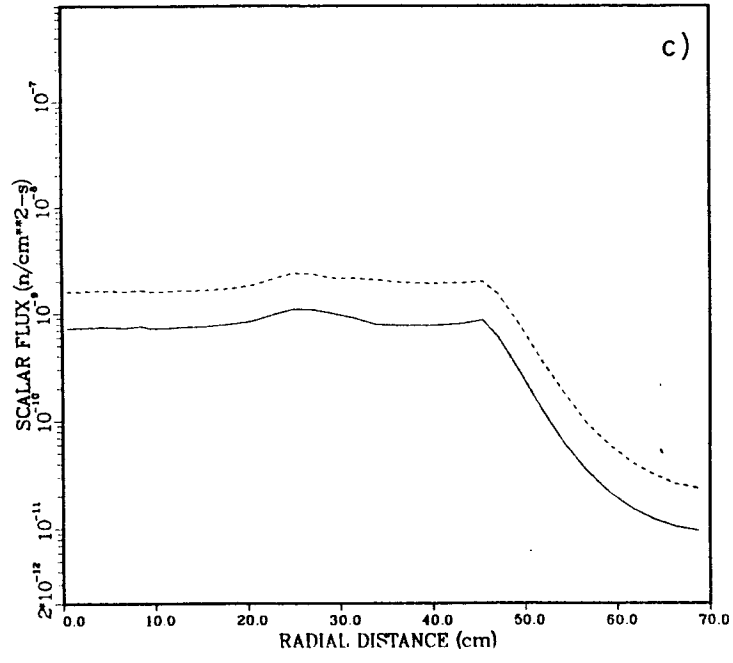

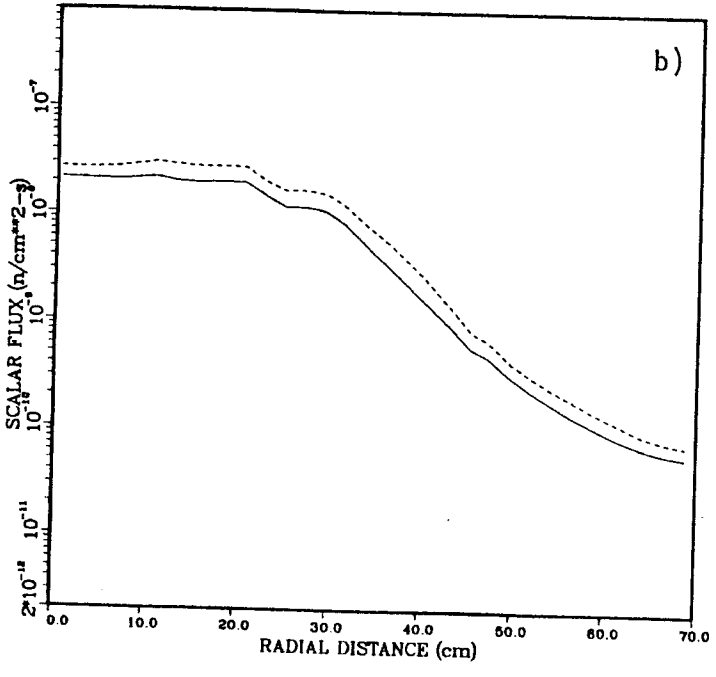

Fig. 15. Radial distribution of the neutron flux in group 20 for three axial positions; a) back of graphite moderator (z = 100 cm), b) front of diode (z = 170 cm), and c) back of diode (z = 210 cm).

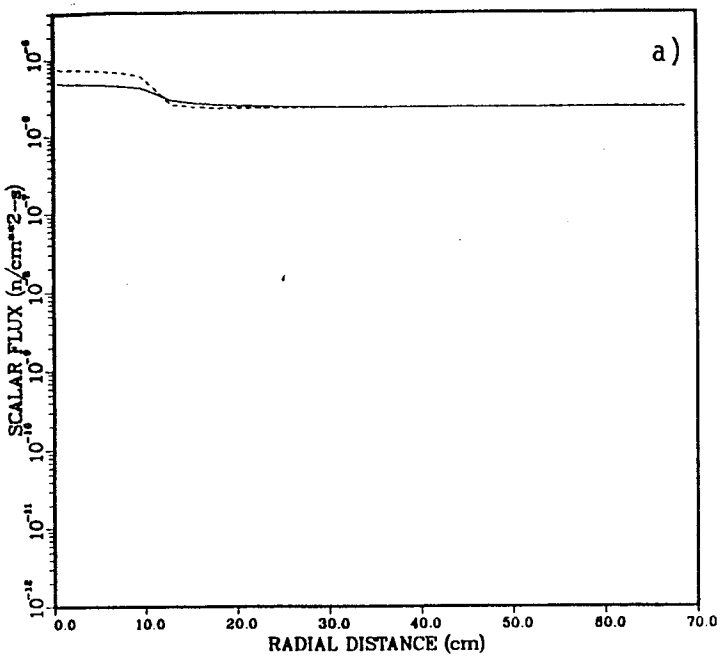

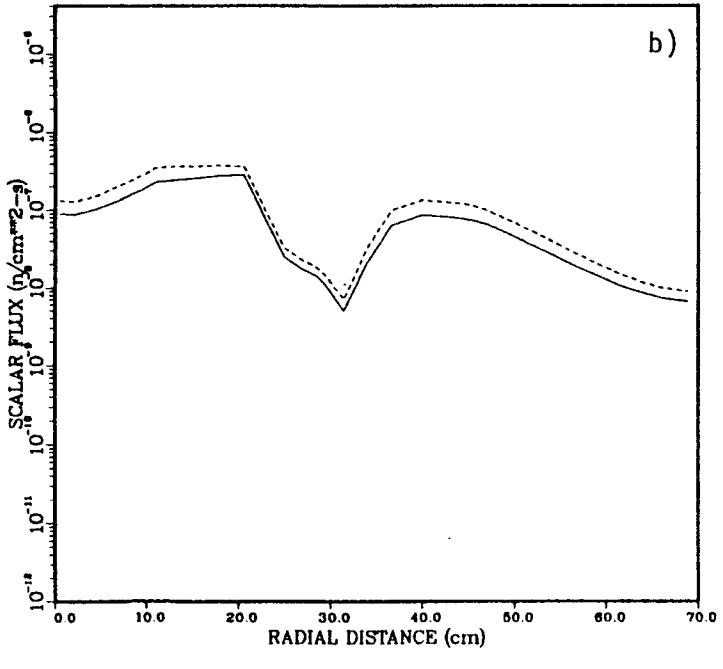

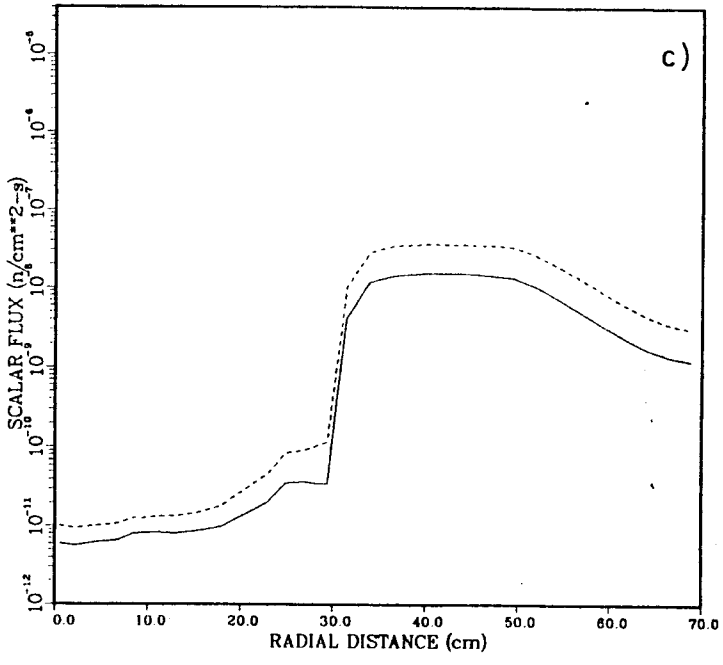

Fig. 16. Radial distribution of the neutron flux in group 30 for three axial positions; a) back of graphite moderator (z = 100 cm), b) front of diode (z = 170 cm), and c) back of diode (z = 210 cm).

cates that using the 30 cm thick moderator will force the 14 MeV neutrons to impinge on the outer parts of the diode resulting in overestimating the dose outside the diode. This effect is less pronounced for energy group 7 due to the smaller contribution from the neutrons coming directly from the target and is negligible for lower energy groups. The structure in the radial distribution of thermal neutrons is due to the radial distribution of the material with the dip around r = 30 cm resulting from attenuation in the front parts of the cathode and Cu coil. It is clear also that the effect of reducing the moderator thickness to 30 cm on the flux at the front of the diode becomes less pronounced for lower energy groups. The structure in the radial distribution at the back of the diode can be related to the distribution of materials in the diode. It is interesting to note that the radial distribution of the flux at the back of the diode is the same for the two moderator thicknesses with the difference in absolute values decreasing for lower energy groups.

3. DOSE RATE CALCULATION

3.1 Method of Solution

The dose rate calculations were performed using the DKR-ICF[15] code package which consists of the radioactivity calculations code DKR, the data handling code CONVERT and the dose rate calculations code DOSE. The spatial model used for the diode calculations is identical to the model used for the TWODANT neutronic calculation and is given in Fig. 10. The large dot drawn next to the diode casing designates the point at which the dose rate is calculated. ACTLLIB, a decay and neutron transmutation data library based on the evaluated neutron activation cross section library, ACTL,[16] is used as the

primary data base for the activation calculations. The neutron transmutation data is given in a 46 group structure format. The decay and gamma source data is taken from the Table of Isotopes[17] with the gamma source data being in a 21 group structure format. Appendix A gives the composition of the materials used in the calculations. The dose rate calculations are dominated by the radioactivity computation which takes approximately 9-10 hours of Cray-XMP time per case.

A new computational model has been developed for the activation calculations to account for the sequential pulse operation mode of the Target Development Facility. Treating the pulsed problem as a time averaged steady state problem can lead to significant errors in the calculated activity and dose. These differences are illustrated here by comparing the analytic expressions for the radioactive nuclide density obtained using pulsed and equivalent steady state irradiation for a simple radioactive decay chain with idealized pulse shape.

Consider a series of n square pulses that have a width δ seconds and are Δ seconds apart as illustrated in Fig. 17. In the analysis performed here, it is assumed that $\Delta >> \delta$. The equivalent steady state neutron flux ϕ_s is related to the flux ϕ_p during the pulse via

$$\phi_s = \frac{\delta}{\Delta} \phi_p \ . \tag{1}$$

It is assumed that neutrons interact with a nuclide of initial concentration $N_0(0)$ with a cross section σ to produce a radioactive nuclide which has a decay constant λ and that it decays into a stable nuclide. Also assumed is that the radioactive nuclide is not further transmuted by neutron capture. The

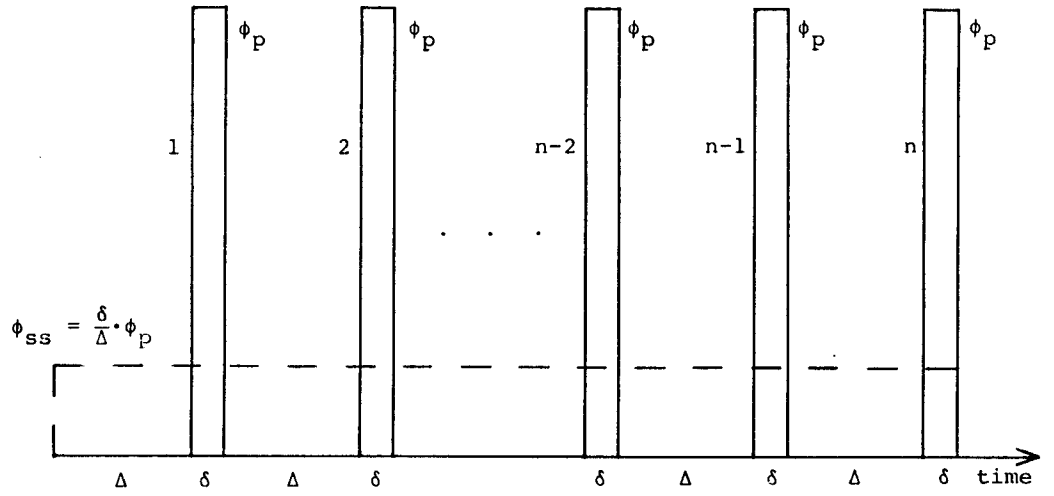

Fig. 17. Relation between the neutron flux during the pulse and the equivalent steady state flux.

concentration of the radioactive nuclide at time t during the operation at a flux level ϕ is given by

$$N(t) = \frac{N_o(0)\ \sigma\phi}{\lambda - \sigma\phi} \left(e^{-\sigma\phi t} - e^{-\lambda t}\right) . \qquad (2)$$

Assuming $\delta << \frac{1}{\lambda}$ and $\frac{1}{\sigma\phi_p}$, N at the end of the first pulse is $N_o(0)\ \sigma\phi_p\delta$. At shutdown (the end of the nth pulse) the contribution from the first pulse will be $N_o(0)\ \sigma\phi_p\delta e^{-(n-1)\lambda\Delta}$. Adding the contributions from the n pulses the concentration of the radioactive nuclide at shutdown is given by

$$N_p = N_o(0)\ \sigma\phi_p\delta e^{-(n-1)\sigma\phi_p\delta} \sum_{i=1}^{n} e^{-(n-1)(\lambda\Delta-\sigma\phi_p\delta)} . \qquad (3)$$

The geometric progression in Eq. (3) reduces to a closed form and N_p is given by

$$N_p = N_o(0)\ \sigma\phi_p\delta\ \frac{[e^{-n\sigma\phi_p\delta} - e^{-n\lambda\Delta}]}{[e^{-\sigma\phi_p\delta} - e^{-\lambda\Delta}]} . \tag{4}$$

Using Eqs. (1) and (2), the corresponding expression for the equivalent steady state case is

$$N_s = \frac{N_o(0)\ \sigma\phi_p\delta}{\lambda\Delta - \sigma\phi_p\delta}\ [e^{-n\sigma\phi_p\delta} - e^{-n\lambda\Delta}] . \tag{5}$$

Equations (4) and (5) imply that

$$\frac{N_p}{N_s} = \frac{\lambda\Delta - \sigma\phi_p\delta}{[e^{-\sigma\phi_p\delta} - e^{-\lambda\Delta}]} . \tag{6}$$

This relation between N_p and N_s will hold at any time after shutdown.

For nuclides with very short half lives ($\lambda\Delta >> 1$) Eq. (6) reduces to

$$\frac{N_p}{N_s} = \lambda\Delta , \tag{7}$$

implying that the steady state calculation will underestimate the activity by a factor of $\lambda\Delta$. On the other hand for very long lived nuclides ($\lambda\Delta << 1$), Eq. (6) reduces to

$$\frac{N_p}{N_s} = 1 . \tag{8}$$

This implies that the equivalent steady state model gives results identical to the actual pulsed case only for very long lived isotopes. The relation between the pulsed and equivalent steady state results gets complicated for non-

uniform pulsing schedules and when decay chains with more than one radioactive nuclide are considered.

The simple example discussed above is extended to determine the activity following a nonuniform pulse schedule as used for TDF. The temporal model as briefly outlined in Fig. 18 computes the production of the radioactive nuclides only during the pulse and allows for decay between pulses. In the example depicted in Fig. 18 the accumulation of the radionuclide for 12 shots per day is given by S_{12}^{D}. Following the operation of the facility for 5 days a week the radionuclide concentration is given by S_{5}^{W}. The yearly accumulation after 52 weeks is given by S_{52}^{Y}. $Q(\delta)$ denotes the production of the radionuclide during the pulse. The underlying assumptions of this model are that the pulse width, δ (time of irradiation), is much smaller than the time between pulses, Δ (i.e., $\delta << \Delta$) and that the destruction of the initial and created isotopes is neglected. A comparison between the pulse sequence and steady state irradiation calculations will be given in Section 3.4.

3.2 Calculation Procedure

The adjoint scheme shown in the flowchart diagram of Fig. 19 is used to compute the dose rates at the diode casing's outer surface (see black dot in Fig. 10) for 12 after shutdown times. Four separate computational steps are required to obtain the dose rates. The first step is the determination of the steady state neutron flux throughout the graphite moderator, aluminum first wall, boral and diode regions using the TWODANT transport code (see Section 2.4). The flux throughout the different regions is used in the second step of the calculation which involves the use of the DKR code to compute material activation resulting from neutron transmutation reactions and the computation of the decay gamma sources. Step three is the determination of the adjoint

DAILY PULSE SEQUENCE

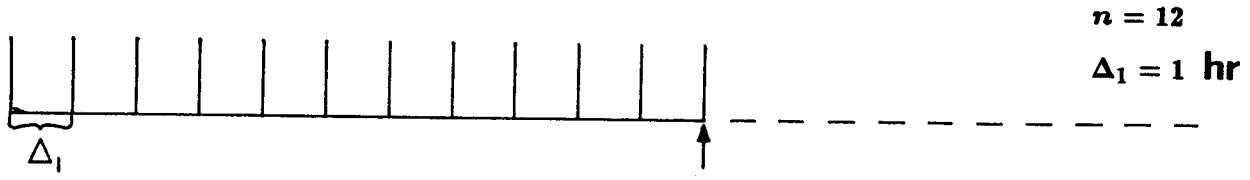

$$S_n^D = Q(\delta)[1 + e^{-\lambda\Delta_1} + e^{-\lambda 2\Delta_1} + e^{-\lambda 3\Delta_1} + e^{-\lambda 4\Delta_1} + e^{-\lambda 5\Delta_1} + \cdots + e^{-\lambda 11\Delta_1}]$$

$$S_n^D = \frac{Q(\delta)(1 - e^{-\lambda\Delta_1 n})}{(1 - e^{-\lambda\Delta_1})} \xrightarrow{n=12} \boxed{S_{12}^D = \frac{Q(\delta)(1-e^{-12\lambda\Delta_1})}{(1-e^{-\lambda\Delta_1})}}$$

WEEKLY PULSE SEQUENCE

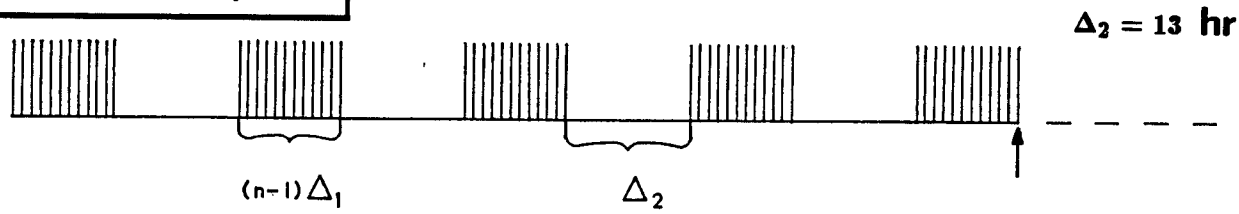

$$S_m^W = S_{12}^D[1 + e^{-\lambda(\Delta_2+(n-1)\Delta_1)} + e^{-\lambda 2(\Delta_2+(n-1)\Delta_1)} + e^{-\lambda 3(\Delta_2+(n-1)\Delta_1)} + e^{-\lambda 4(\Delta_2+(n-1)\Delta_1)}]$$

$$S_m^W = S_{12}^D \frac{(1 - e^{-\lambda m(\Delta_2+(n-1)\Delta_1)})}{(1 - e^{-\lambda(\Delta_2+(n-1)\Delta_1)})} \xrightarrow[m=5]{n=12} \boxed{S_5^W = S_{12}^D \frac{(1-e^{5\lambda(\Delta_2+11\Delta_1)})}{(1-e^{-\lambda(\Delta_2+11\Delta_1)})}}$$

YEARLY PULSE SEQUENCE

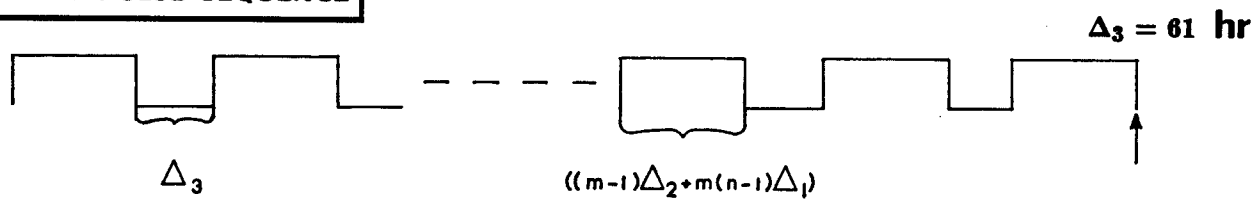

$$S_l^Y = S_5^W[1 + e^{-\lambda(\Delta_3+(m-1)\Delta_2+m(n-1)\Delta_1)} + e^{-\lambda 2(\Delta_3+(m-1)\Delta_2+m(n-1)\Delta_1)} + \cdots + e^{-\lambda 51(\Delta_3+(m-1)\Delta_2+m(n-1)\Delta_1)}]$$

$$S_l^Y = S_5^W \frac{(1 - e^{-\lambda l(\Delta_3+(m-1)\Delta_2+m(n-1)\Delta_1)})}{(1 - e^{-\lambda(\Delta_3+(m-1)\Delta_2+m(n-1)\Delta_1)})} \xrightarrow[m=5]{n=12} \boxed{S_{52}^Y = S_5^W \frac{1-e^{-52\lambda(\Delta_3+4\Delta_2+55\Delta_1)}}{(1-e^{-\lambda(\Delta_3+4\Delta_2+55\Delta_1)})}}$$

ASSUMPTIONS: **Time of irradiation << time between pulses**
Neglect burnup of initial and created nuclides

Fig. 18. Temporal model to account for the sequential pulse operation mode of the Target Development Facility.

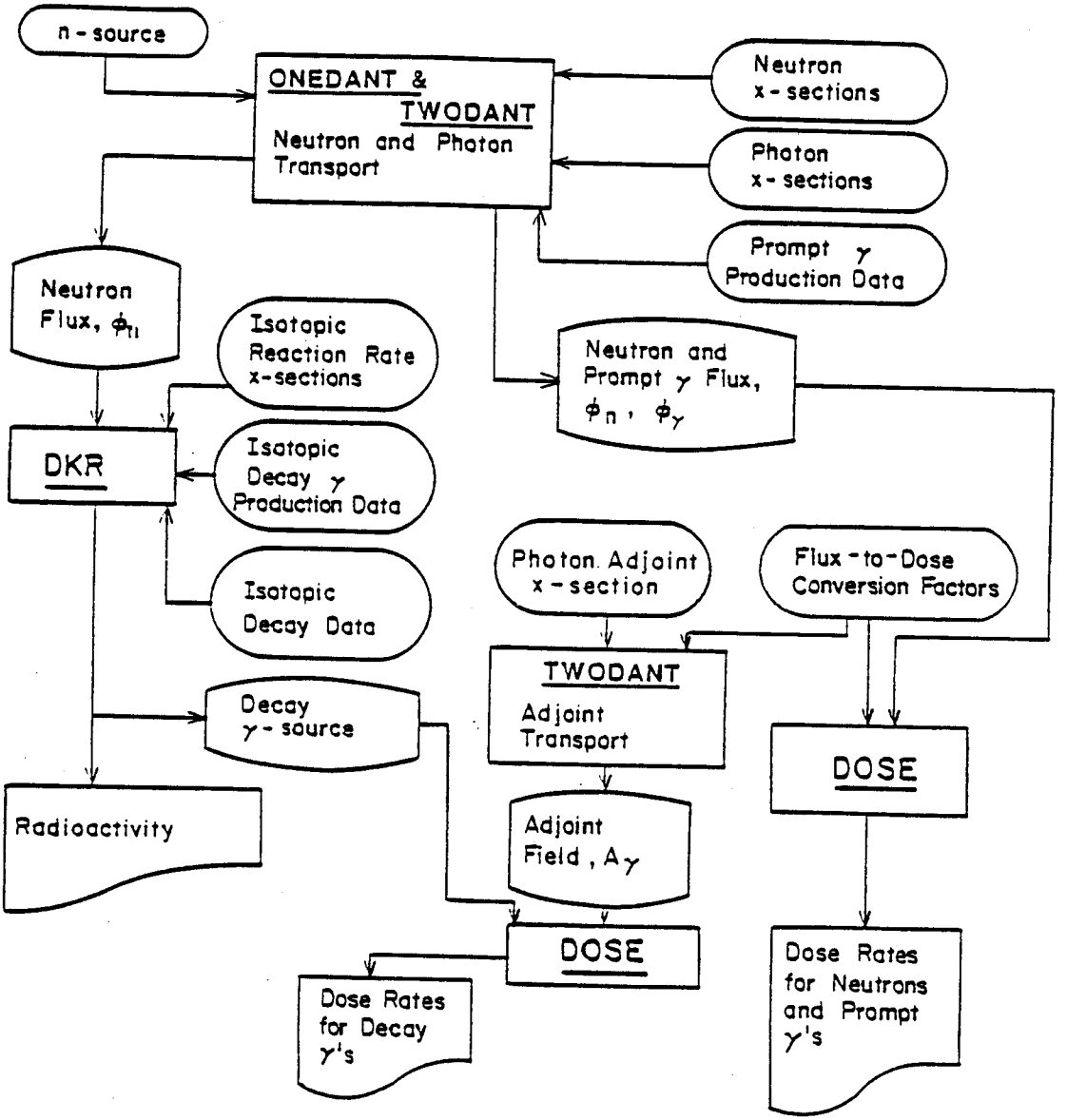

Fig. 19. Flowchart for the calculation of dose rates for the Target Development Facility using the adjoint scheme.

dose field throughout the facility using the TWODANT transport code and the flux-to-dose rate conversion factors.[18] The fourth and final step is the multiplication of the adjoint field by the gamma decay sources using the DOSE code to obtain the dose rate at the outer surface of the diode casing. The gamma source input data to DOSE is prepared by an auxiliary data handling program, CONVERT, which rewrites the DKR created binary gamma source file into a FIDO formatted gamma source file required for DOSE.

3.3 Pulse Sequence Diode Dose Rate Results

Due to the approximately 9-10 hours of Cray running time for the activation calculations, not all of the different diode material, penetration size and solution mode options could be calculated. Table 1 presents the different options and indicates the ones for which dose rates were computed.

The dose rate results are normalized to 200 MJ of target yield. The operational pulse sequence is assumed to be 12 shots per day for 5 days per week for 4 weeks corresponding to a steady state operation time of approximately 1 month. The dose contributions from all components other than from the graphite moderator (for which the contribution is small) are to be determined relative to the diode casing's outer surface (see Fig. 10).

The pulse sequence mode dose rate results at the diode casing's outer surface for a 10 cm radius penetration and for different diode materials are shown in Fig. 20. For short times after shutdown (up to ~ 2 days) one clearly notes that the aluminum dose rates exceed the stainless steel dose rates. Thereafter the stainless steel rates exceed the aluminum rates up to ~ 70 years after shutdown at which time the dose levels have become negligibly small. Since the surrounding structure and water shield are identical for both diode materials, the difference between the curves is solely due to

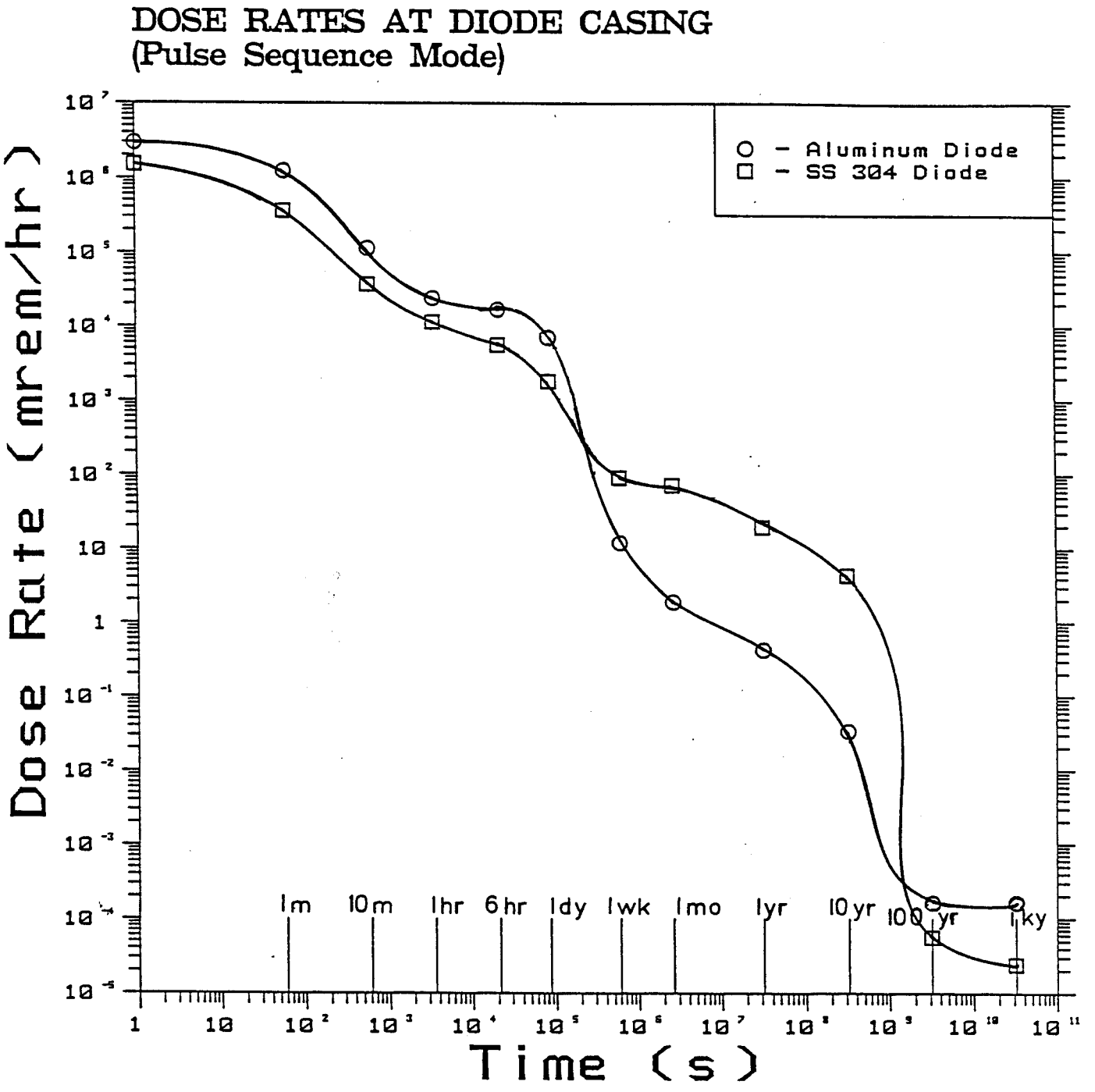

Fig. 20. A comparison of the aluminum diode and stainless steel (including surrounding structural material and water shield) dose rates at the diode casing's outer surface using the pulse sequence model.

Table 1. Four Different Diode and Penetration Options

	Case 1	Case 2	Case 3	Case 4
Diode material	SS 304LN	Al-6061-T6	SS 304LN	Al-6061-T6
Radius of graphite moderator penetration	10 cm	10 cm	1 cm	1 cm
Pulsed dose calculation	yes	yes	no	no
Steady state dose calculation	yes	yes	yes	no

transmutation and activation response of each diode material. The initial shape of both curves up to approximately 1 day after shutdown exhibits the same behavior and is determined by the decay of the short-lived isotopes, $^{28}_{13}Al$, $^{30}_{13}Al$, $^{27}_{12}Mg$, $^{26}_{11}Na$ and $^{24}_{11}Na$ produced in the aluminum components. The addition of the aluminum diode dose contribution to that of the surrounding aluminum components accounts for the difference in magnitude up to 1 day after shutdown. The large drop in the aluminum diode dose level from 7.04 rem/hr at 1 day to 12 mrem/hr at 1 week after shutdown is the result of the decay of $^{24}_{11}Na$ which has a half-life of 15 hours. $^{24}_{11}Na$ is produced by a (n,α) reaction on $^{27}_{13}Al$. During the same time interval the stainless steel diode dose level drops from 1.8 rem/hr to 90 mrem/hr. The decay of $^{24}_{11}Na$ is again the cause for this drop. The crossover point occurs approximately 2-3 days after shutdown with the stainless steel diode dose exceeding the aluminum diode dose level for nearly 70 years. One must wait approximately 3 days after shutdown for the aluminum case and 5 days after shutdown for the stainless steel case before the dose levels drop below 100 mrem/hr. The values for the points

plotted are given in Table 2. Table 3 contains the radionuclides which produce approximately 90% of the gamma photons for various times after shutdown.

The various components that contribute to the total dose rate at the outer surface of the diode casing are the aluminum first wall, boral lining, plastic insulator, copper coils, aluminum casing (including rotating shutters), water shield and diode material. The dose rate contribution of these components is plotted in Fig. 21 for the stainless steel diode case. The $^{16}_{7}N$ with a half-life of 7.10 s is produced in the plastic and water shield and decays to negligible levels within 4-5 minutes after shutdown. As expected, the components containing a high weight percent of aluminum (boral, aluminum first wall and casing) follow the same decay behavior. The aluminum first wall and casing components have a nearly equivalent contribution to the total dose level except for slight differences at early times and in the range 1 day to 1 year after shutdown. This is related to the difference in the neutron energy spectrum in the different zones. The contribution of the boral layers is approximately one order of magnitude lower than the aluminum first wall contribution. Clearly noticeable is the point at which the stainless steel diode component begins to dominate the dose levels. One could imagine removing the diode by remote means at this point to take advantage of the significant drop in the dose contribution of the aluminum components between 1 day and 1 week after shutdown. The decay of $^{24}_{11}Na$ during this time interval would allow hands on maintenance at the casing's outer surface 1 week after shutdown. Remote handling of the stainless steel diode itself is still required as the dose level does not drop below 50 mrem/hr until 2 months after shutdown. The copper coil dose contribution is 2 to 3 orders of magnitude lower

Table 2. Aluminum 6061-T6 and SS 304LN Dose Rate Results for Both the Pulse Sequence and Steady State Modes and for a 10 cm Radius Penetration [mrem/hr]

Time	Stainless Steel 304LN		Aluminum 6061-T6	
	Pulse Sequence Mode	Steady State Mode	Pulse Sequence Mode	Steady State Mode
At Shutdown	1.50×10^{6}	1.59×10^{4}	2.98×10^{6}	4.78×10^{4}
1 m	3.59×10^{5}	1.24×10^{4}	1.24×10^{6}	3.81×10^{4}
10 m	3.68×10^{4}	6.02×10^{3}	1.13×10^{5}	1.55×10^{4}
1 hr	1.12×10^{4}	4.78×10^{3}	2.38×10^{4}	1.22×10^{4}
6 hr	5.58×10^{3}	2.75×10^{3}	1.70×10^{4}	9.15×10^{3}
1 dy	1.80×10^{3}	1.03×10^{3}	7.04×10^{3}	3.86×10^{3}
1 wk	90.0	85.5	12.0	7.74
1 mo	71.0	68.6	1.91	1.85
1 yr	19.5	19.0	4.32×10^{-1}	4.24×10^{-1}
10 yr	4.37	4.24	3.42×10^{-2}	3.33×10^{-2}
100 yr	5.56×10^{-5}	5.58×10^{-5}	1.65×10^{-4}	1.62×10^{-4}
1000 yr	2.41×10^{-5}	2.52×10^{-5}	1.65×10^{-4}	1.61×10^{-4}

Table 3. Important Gamma-Photon Producing Isotopes

Stainless Steel 304 Diode

Time 0	1 hr	1 day	1 week	1 month	1 yr
Al-28	Cr-51	Cr-51	Cr-51	Cr-51	Mn-54
V-52	Mn-56	Mn-54	Mn-54	Mn-54	Co-58
Mn-56		Co-58	Co-58	Co-58	Co-60
Al-30		Co-58	Co-57	Co-57	Co-57

Aluminum Diode

Time 0	1 hr	1 day	1 week	1 month	1 yr
Na-24	Na-24	Na-24	Na-24	Cr-51	Mn-54
Na-26	Mg-27	Cu-64	Cr-51	Mn-54	Zn-65
Mg-27	Mn-56		Mn-54	Zn-65	
Al-28	Cu-64		Zn-65		
Al-30					

Water Shield

Time 0	1 hr	1 day	1 week	1 month	1 yr
N-16	---	---	---	---	---

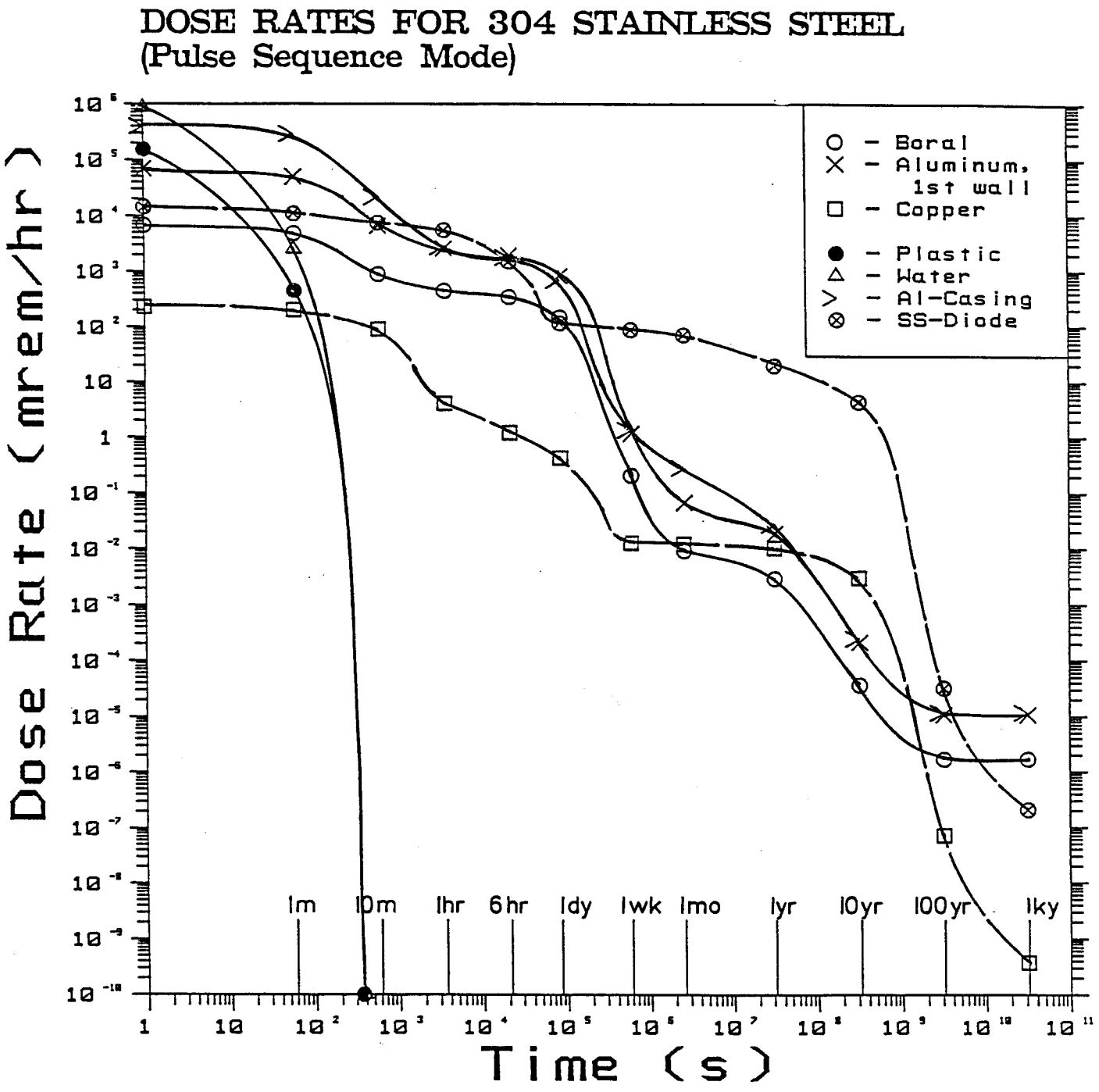

Fig. 21. The dose rate contribution of the various structural and shield materials to the total stainless steel dose rate using the pulse sequence model and a penetration radius of 10 cm.

than for the stainless steel and thus its contribution to the total dose rate is small. Table 4 contains the dose values plotted in Fig. 21.

The dose level contributions of the various components compromising the aluminum case are shown in Fig. 22. Noticeable again is the decay of $^{16}_{7}N$ produced in the plastic and water shield. For the aluminum diode case, the contribution from the diode itself dominates the dose rate and is approximately one order of magnitude larger than the contribution from either the aluminum first wall or the aluminum casing. The contribution from the boral layers is as in the stainless steel, approximately one order of magnitude lower than that from the aluminum first wall. Since the dose level from the aluminum diode component drops considerably between 1 day and 1 week after shutdown, removal of the diode and diode casing accessibility do not constitute a major hazard. Hands on maintenance of the diode and the diode casing's outer surface is possible 1 week after shutdown. The copper coil dose contribution is lower than the aluminum diode level except in the time interval ~ 2-70 years after shutdown. Table 5 contains the dose values plotted in Fig. 22.

Another point to note is the effect the diode material has on the embedded copper coil dose contribution. For the aluminum diode case the copper dose contribution is approximately one order of magnitude larger than for the stainless steel diode case. This is attributed to inelastic scattering in the Fe contained in the stainless steel which depresses the high energy flux within the diode.

For both the aluminum and stainless steel cases that are examined the dose rates at the diode casing's outer surface are above 1 rem/hr at 1 day after shutdown. At approximately 3 days after shutdown for the aluminum case and 5 days after shutdown for the stainless steel case the dose level has

Table 4. Component Dose Rates for the SS 304LN Diode Computation [mrem/hr]

	Component						
Time	Boral	Al-First Wall	Copper	Plastic	Water	Al-Casing	SS-Diode
At Shutdown	6.75×10^{3}	6.94×10^{4}	2.27×10^{2}	1.53×10^{5}	8.66×10^{5}	3.94×10^{5}	1.44×10^{4}
1 m	4.88×10^{3}	5.05×10^{4}	2.01×10^{2}	4.49×10^{2}	2.55×10^{3}	2.89×10^{5}	1.11×10^{4}
10 m	8.92×10^{2}	6.55×10^{3}	90.5	7×10^{-21}	4×10^{-20}	2.19×10^{4}	7.45×10^{3}
1 hr	4.49×10^{2}	2.55×10^{3}	4.02	---	---	2.74×10^{3}	5.74×10^{3}
6 hr	3.46×10^{2}	1.95×10^{3}	1.19	---	---	1.78×10^{3}	1.51×10^{3}
1 dy	1.49×10^{2}	8.34×10^{2}	4.22×10^{-1}	---	---	6.99×10^{2}	1.17×10^{2}
1 wk	2.05×10^{-1}	1.17	1.25×10^{-2}	---	---	1.35	87.2
1 mo	9.24×10^{-3}	6.68×10^{-2}	1.20×10^{-2}	---	---	2.76×10^{-1}	70.6
1 yr	2.91×10^{-3}	1.87×10^{-2}	1.01×10^{-2}	---	---	2.66×10^{-2}	19.5
10 yr	3.57×10^{-5}	2.15×10^{-4}	2.96×10^{-3}	---	---	2.46×10^{-4}	4.37
100 yr	1.69×10^{-6}	1.07×10^{-5}	7.13×10^{-8}	---	---	1.15×10^{-5}	3.17×10^{-5}
1000 yr	1.69×10^{-6}	1.07×10^{-5}	3.67×10^{-10}	---	---	1.15×10^{-5}	2.10×10^{-7}

Table 5. Component Dose Rates for the Aluminum 6061-T6 Diode Computation [mrem/hr]

Time	Component						
	Boral	Al-First Wall	Copper	Plastic	Water	Al-Casing	Al-Diode
At Shutdown	9.00×10^{3}	8.94×10^{4}	3.21×10^{3}	2.01×10^{5}	1.09×10^{6}	6.25×10^{5}	9.67×10^{5}
1 m	6.51×10^{3}	6.51×10^{4}	2.87×10^{3}	5.89×10^{-2}	3.19×10^{3}	4.58×10^{5}	7.07×10^{5}
10 m	1.20×10^{3}	8.61×10^{3}	1.31×10^{3}	1×10^{-20}	5×10^{-2}	3.40×10^{4}	6.83×10^{4}
1 hr	5.94×10^{2}	3.34×10^{3}	6.12×10^{1}	---	---	3.83×10^{3}	1.60×10^{4}
6 hr	4.58×10^{2}	2.55×10^{3}	2.08×10^{1}	---	---	2.41×10^{3}	1.15×10^{4}
1 dy	1.97×10^{2}	1.09×10^{3}	7.57	---	---	9.26×10^{2}	4.82×10^{3}
1 wk	2.73×10^{-1}	1.54	1.36×10^{-1}	---	---	1.94	8.06
1 mo	1.36×10^{-2}	9.63×10^{-2}	1.29×10^{-1}	---	---	4.57×10^{-1}	1.21
1 yr	4.31×10^{-3}	2.72×10^{-2}	1.08×10^{-1}	---	---	3.78×10^{-2}	2.55×10^{-1}
10 yr	5.05×10^{-3}	2.99×10^{-4}	3.15×10^{-2}	---	---	3.39×10^{-4}	1.98×10^{-3}
100 yr	2.38×10^{-6}	1.50×10^{-5}	1.15×10^{-6}	---	---	1.51×10^{-5}	1.31×10^{-4}
1000 yr	2.37×10^{-6}	1.50×10^{-5}	6.80×10^{-9}	---	---	1.51×10^{-5}	1.31×10^{-4}

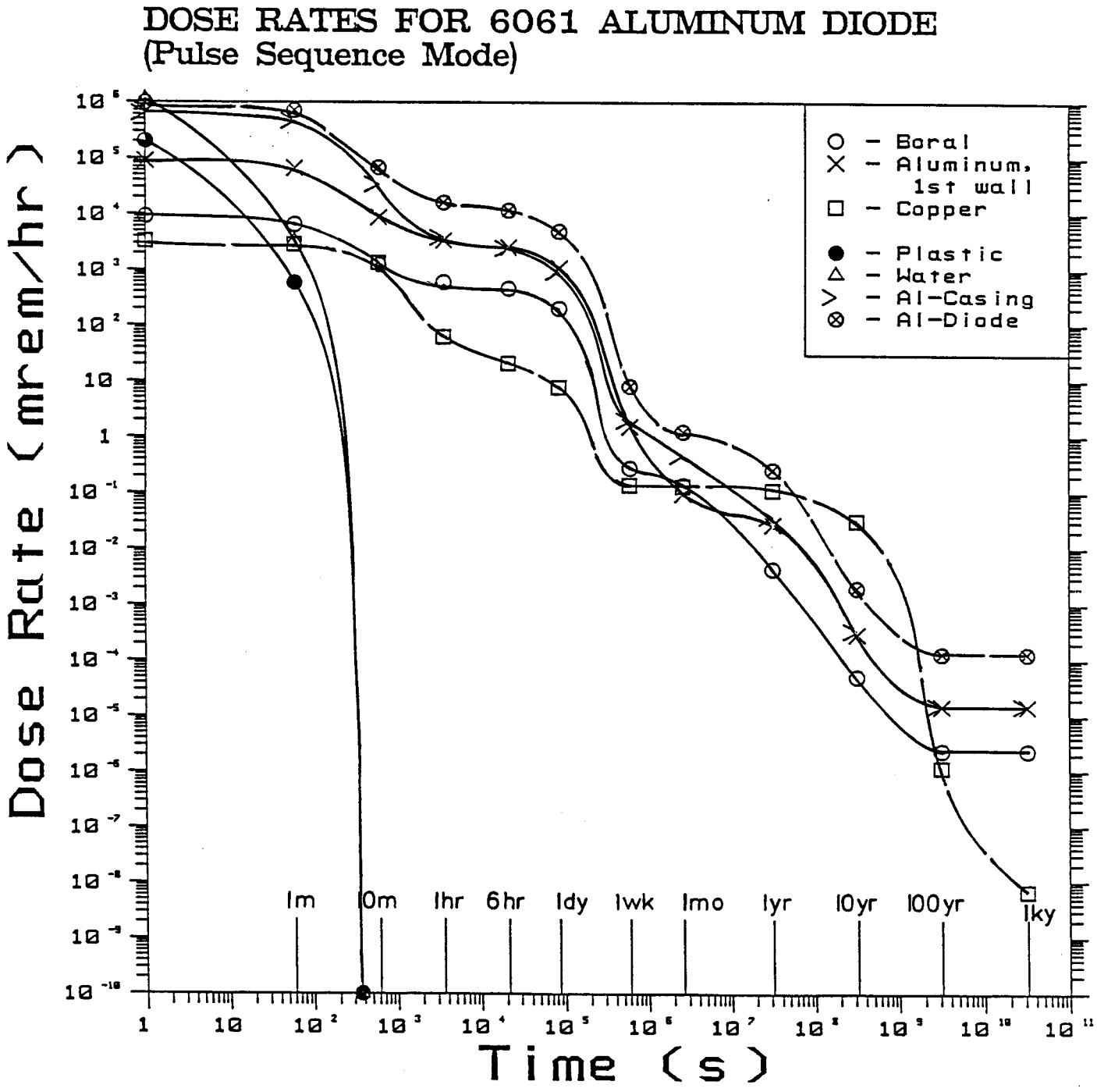

Fig. 22. The dose rate contribution of the various structural and shield materials to the total aluminum dose rate using the pulse sequence model and a penetration radius of 10 cm.

dropped to 100 mrem/hr. Thereafter the dose level drops to 90 mrem/hr for the stainless steel case and 12 mrem/hr for the aluminum case at 1 week after shutdown. Thus, waiting longer than 1 week after shutdown to remove the stainless steel diode is not beneficial as the dose level does not drop below 50 mrem/hr until 2 months after shutdown. Here, remote removal and examination of the diode itself may be necessary with limited hands on maintenance being a possibility. Once the diode has been removed, access to the diode casing is possible after a 1 week shutdown period. For the aluminum diode case waiting until 1 week after shutdown is advantageous as the dose level is considerably reduced. There is a possibility for manual (hands on) removal and examination of the diode.

Note that the above analysis does not take into account increases in the dose level due to sky shining once the water has been removed or streaming of decay gammas down the beam lines once the diode has been removed. These cases should also be addressed at some point during the design.

3.4 Pulse Sequence Operation Versus Steady State Operation

Earlier in Section 3.1 the underlying assumptions of the pulse sequence operational model (a more realistic model of the facility's operation) were discussed. In this section a brief comparison of the pulse sequence and steady state operation modes is discussed.

In Figs. 23 and 24 a comparison of the results of the pulse sequence and steady state calculations for the stainless steel and aluminum cases are given. For the stainless steel case the curves coalesce at approximately 5 days after shutdown whereas for the aluminum case the curves coalesce at approximately 13-14 days after shutdown. Since the surrounding structural and water shield components are identical, the difference in the time at which the

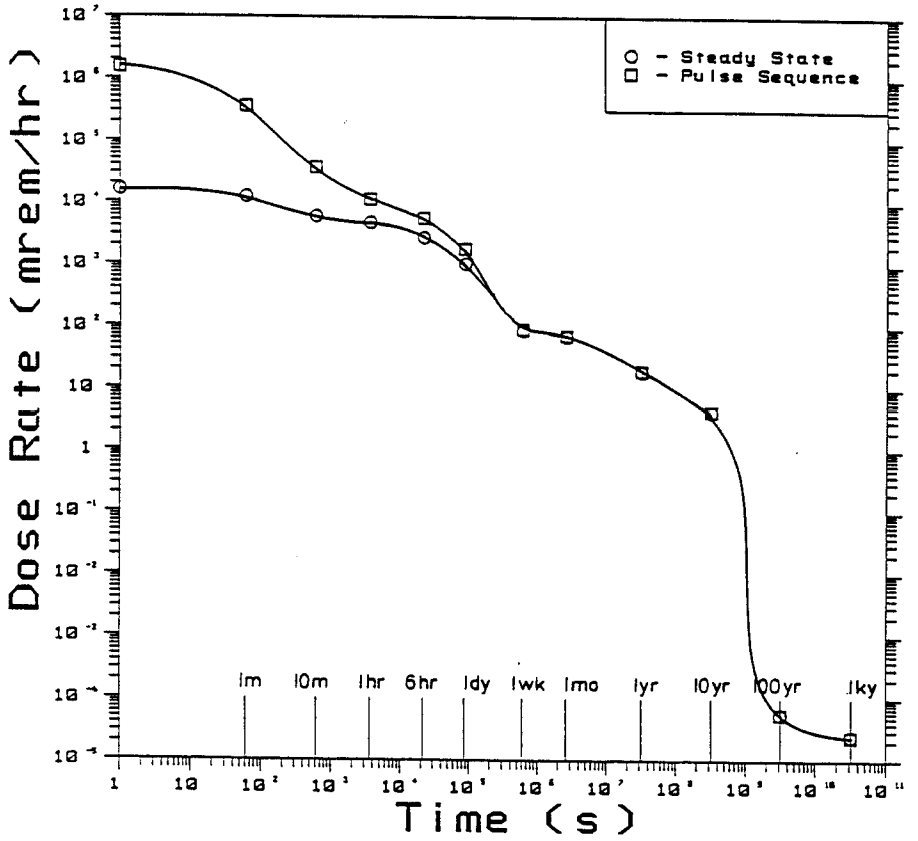

Fig. 23. A comparison of the pulse sequence and steady state calculational models for stainless steel using a penetration radius of 10 cm.

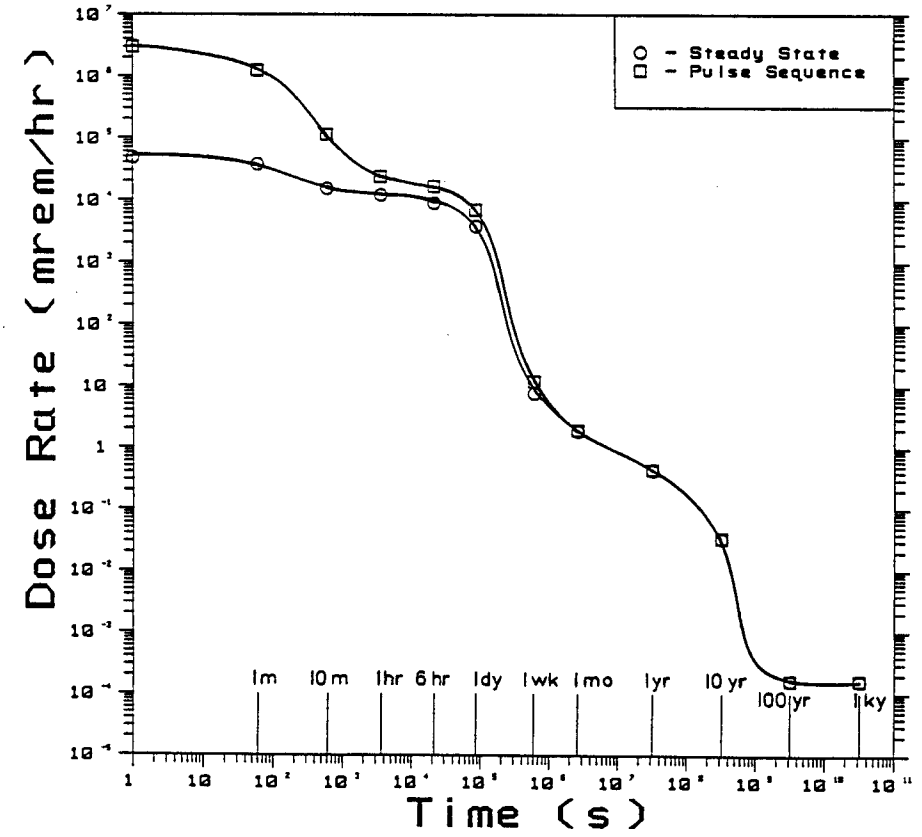

Fig. 24. A comparison of the pulse sequence and steady state calculational models for aluminum using a penetration radius of 10 cm.

steady state and pulse sequence curves merge is the result of the difference in activation of the diode materials. Specifically, this is mainly the result of the production of $^{54}_{25}Mn$ and $^{51}_{24}Cr$ in both diode materials relative to the production of $^{24}_{11}Na$ in the aluminum diode and surrounding structural components. With the half-lives of $^{54}_{25}Mn$ and $^{51}_{24}Cr$ being 27.7 days and 312.5 days, respectively, which are much larger than the largest spacing between pulses (61 hours), their decay rates are not affected by the pulse sequence. On the other hand, the $^{24}_{11}Na$ which has a 15 hour half-life is affected by the 13 hour shutdown period between daily shot sequences. Hence, the curves begin to merge when $^{54}_{25}Mn$ and $^{51}_{24}Cr$ begin to dominate the total dose level. Since the stainless steel diode has a much larger content of Cr and Fe which are the main producers of $^{54}_{25}Mn$ and $^{51}_{24}Cr$, one would expect a larger production of these radionuclides in the stainless steel diode case than in the aluminum diode case. Thus the stainless steel diode results coalesce at an earlier time than the aluminum diode results. For the aluminum diode case, the curves begin to merge as the contribution of the $^{24}_{11}Na$ to the total dose level drops considerably and the longer lived radionuclides, $^{54}_{25}Mn$ and $^{51}_{24}Cr$, begin to dominate the dose level. Table 2 contains the dose values plotted in Figs. 23 and 24.

3.5 Effect of the Discrete Ordinates Calculation and Penetration Opening Size on the Dose Levels

As mentioned in Section 2.4, a shortcoming of the discrete ordinates method is the problem of ray effects for singular sources and particles streaming into void regions. Figure 25 shows a comparison of the 100 cm and 30 cm graphite moderator calculations using the stainless steel diode case and the steady state operation assumption. The difference is at most a factor of

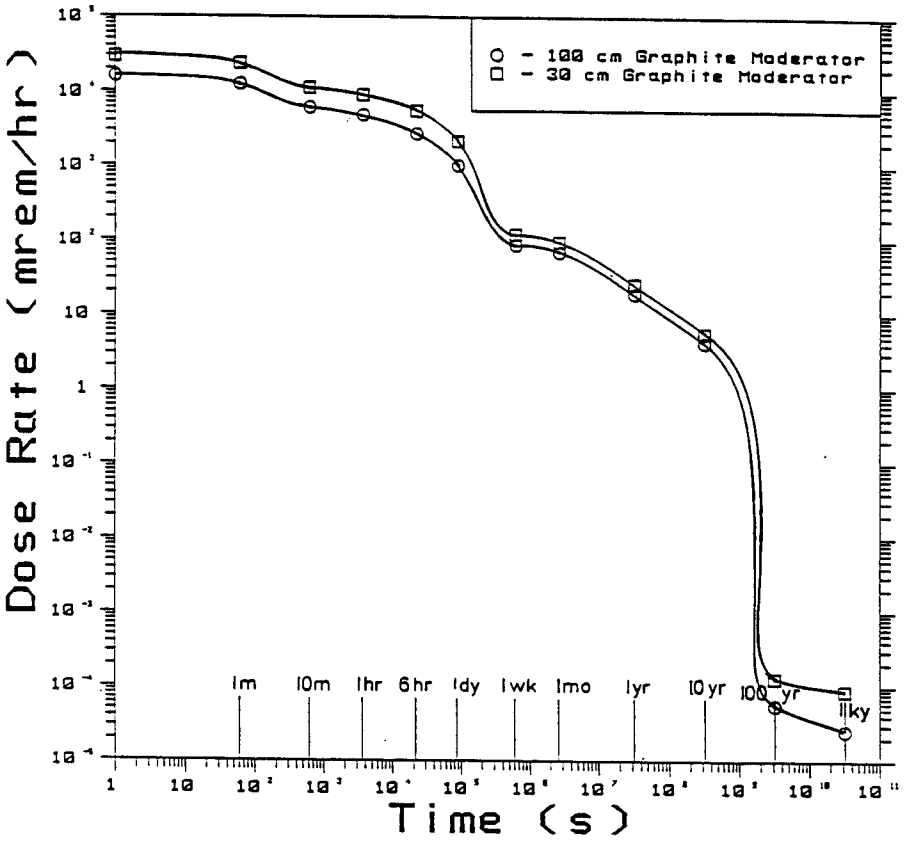

Fig. 25. A comparison of the 100 cm and 30 cm graphite moderator dose rate calculations using the steady state model and a penetration radius of 10 cm.

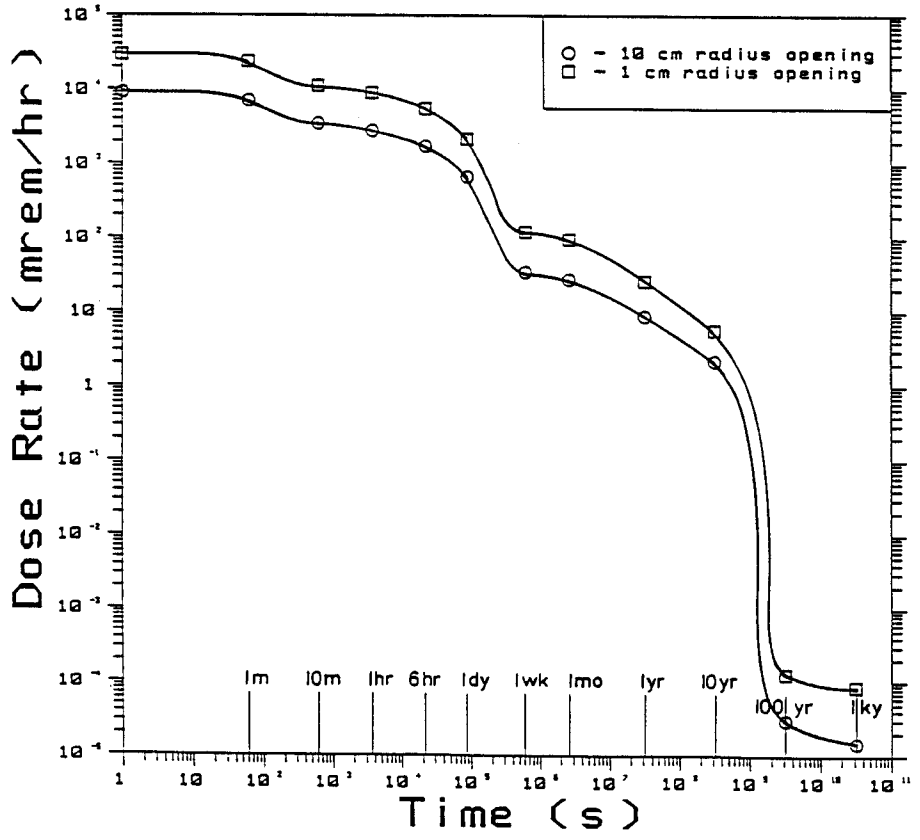

Fig. 26. A comparison of the 1 cm and 10 cm penetration radii using the steady state model and the stainless steel diode.

2. This is a direct result of ~ 2.5 increase in the flux streaming into the diode region as discussed in Section 2.4.

One notices that the difference is greater for times up to 1 day after shutdown than for times in the range 1 week-100 years after shutdown. This is related to the energy spectrum of the neutrons streaming into the diode region and to the discrete ordinates quadrature angle at which the neutrons are forced to stream for the 30 cm graphite moderator case.

The comparison between the dose levels for the 1 cm and 10 cm radius penetrations is shown in Fig. 26. The 30 cm thick graphite moderator results are used for the 10 cm radius penetration case. The difference between the results varies by a factor of 2.5-6 depending on the time after shutdown. This again is related to the estimated factor of ~ 6 larger neutron flux streaming into the diode for the 10 cm radius penetration as discussed in Section 2.4. Table 6 contains the dose values plotted in Figs. 25 and 26.

3.6 Upper Bound Estimates for the Biological Dose Rates

In Section 3.3 the pulse sequence dose rate results were reported for the stainless steel and aluminum diode cases for a 10 cm radius penetration. These calculations were performed with the 100 cm thick graphite moderator which, as discussed in Section 2.4, has the discrete ordinates ray effect shortcoming. In Section 3.5 an estimate of the enhancement of the stainless steel dose levels resulting from the ray effect was obtained by considering a 30 cm thick graphite moderator (see Section 2.4). The steady state irradiation assumption was used for the comparison. Having obtained an estimate of the dose rate enhancement factor in Section 3.5, an upper bound for the dose rates at the diode casing's outer surface is computed. A factor of 2 was chosen for times up to 1 day after shutdown, a factor of 1.35 for times in the

Table 6. SS 304LN Steady State Dose Rate Results for the 100 cm Thick Graphite Moderator with Penetration Radii of 10 cm and 1 cm and for the 30 cm Thick Compressed Graphite Moderator with a 10 cm Radius Penetration [mrem/hr]

Time	30 cm Thick, Compressed Graphite Moderator With Penetration Radius of 10 cm	100 cm Thick Graphite Moderator With Penetration Radius of 10 cm	100 cm Thick Graphite Moderator With Penetration Radius of 1 cm
At Shutdown	2.90×10^{4}	1.39×10^{4}	9.00×10^{3}
1 m	2.31×10^{4}	1.24×10^{4}	6.96×10^{3}
10 m	1.11×10^{4}	6.02×10^{3}	3.47×10^{3}
1 hr	6.85×10^{3}	4.78×10^{3}	2.80×10^{3}
6 hr	5.49×10^{3}	2.75×10^{3}	1.73×10^{3}
1 dy	2.14×10^{3}	1.03×10^{3}	6.70×10^{2}
1 wk	1.19×10^{2}	85.5	33.9
1mo	94.3	68.6	27.1
1 yr	25.3	19.0	8.68
10 yr	5.57	4.24	2.16
100 yr	1.27×10^{-4}	5.58×10^{-5}	3.04×10^{-5}
1000 yr	8.73×10^{-5}	2.52×10^{-5}	1.48×10^{-5}

range 1 week-100 years and a factor of 2.5 for 1000 years after shutdown. The upper bound dose rates for the pulse sequence mode are given in Table 7.

The upper bound estimates do not qualitatively change the requirements for the handling and maintenance of the activated diode. The stainless steel diode still would require remote removal and handling for times up to 2.5 months after shutdown. With the diode removed, the diode casing is accessible at 1 week after shutdown. For the aluminum diode, the possibility still exists for manual (hands on) removal and examination of the diode.

4. SUMMARY

The neutronics calculations for determining the neutron flux in the diode components required for the dose rate calculations have been performed in three steps. Target neutronics calculations were performed to yield the target neutron spectrum which was used as a source in the one-dimensional target chamber calculations. The energy and angle distributions of the neutrons incident on the inner surface of the chamber were then used to represent a surface source in the two-dimensional calculations for the diode. The streaming neutrons at the back of the diode are a factor of ~ 3.5 higher for the aluminum diode than for the steel diode implying more attenuation and activation in the steel diode. The ray effect problem associated with the discrete ordinates method was assessed by performing a calculation with a reduced graphite moderator thickness to force neutrons incident on the penetration opening in the first quadrature direction to stream directly to the diode. This leads to an upper bound for the diode dose levels and results in a factor of ~ 3 more neutrons streaming at the back of the steel diode for a 10 cm radius penetration.

Table 7. Aluminum 6061-T6 and SS 304LN Upper Bound Dose Rate Results for the Pulse Sequence Mode and for a 10 cm Radius Penetration [mrem/hr]

Time	Stainless Steel 304LN	Aluminum 6061-T6
At Shutdown	3.0×10^{6}	6.0×10^{6}
1 m	7.2×10^{5}	2.5×10^{6}
10 m	7.4×10^{4}	2.2×10^{5}
1 hr	2.2×10^{4}	4.8×10^{4}
6 hr	1.1×10^{4}	3.4×10^{4}
1 dy	3.6×10^{3}	1.4×10^{4}
1 wk	1.8×10^{2}	16.2
1 mo	1.4×10^{2}	2.6
1 yr	39.0	5.8×10^{-1}
10 yr	8.8	4.6×10^{-2}
100 yr	1.2×10^{-4}	4.0×10^{-4}
1000 yr	6.0×10^{-5}	4.0×10^{-4}

A new computational model has been developed for the radioactivity and biological dose rate calculation which uses a more realistic pulse sequence scheme to account for the actual pulsed operation of the Target Development Facility. The biological dose rates were computed for a point external to the diode casing following an operational period of 1 month. For the pulse sequence computation it was shown that for both the stainless steel and aluminum diodes the dose rates at the diode casing's outer surface are above 1 rem/hr at 1 day after shutdown. The major contribution to the dose levels at the outer surface comes from the diode material component itself. At 1 week after shutdown the dose levels have dropped to 90 and 12 mrem/hr, respectively. This requires remote handling of the stainless steel diode both for removal and for examination. Once the diode has been removed, access to the diode casing is possible at 1 week after shutdown. For the aluminum diode there is a possibility for manual removal and examination of the diode at 1 week after shutdown.

An upper bound to the biological dose rates was computed using the results of the 30 cm thick compressed graphite moderator case. It was concluded that the estimates do not qualitatively change the requirements for the handling and maintenance of the activated diode and diode casing.

ACKNOWLEDGEMENTS

Support for this work has been provided by Sandia National Laboratories under contract #59-3149. Computer time was provided by the National Science Foundation at the San Diego Supercomputer Center on a Cray-XMP/48. The authors wish to thank Dr. Hosny Attaya for his help in implementing the neutronics codes on the SDSC Cray and for his CFTLIB-FORTLIB file translation program. Also his helpful advice during the early running stages of the DKR radioactivity code on the SDSC Cray is greatly appreciated.

APPENDIX A:

The Appendix contains the composition of the various materials used for the diode neutron transport and dose rate calculation.

Table A.1. Composition of Materials Comprising the Diode, First Wall, Boral, Graphite Liner and Graphite Moderator Regions

Element (wt.%)	Oxygen Free-High[19] Conductivity Copper ρ = 8.96 g/cm^3	SS 304LN[20] ρ = 8.03 g/cm^3	Al-6061-T6 ρ = 2.7 g/cm^3
H	0.0002	---	---
B	---	---	---
C	---	0.022	---
N	---	0.149	---
O	0.0003	---	---
Mg	---	---	1.0
Al	---	---	96.55
Si	---	0.62	0.60
P	0.0003	0.019	---
S	0.002	0.005	---
Ti	---	---	0.15
V	---	---	---
Cr	---	18.31	0.30
Mn	0.00004	1.33	0.15
Fe	0.001	69.73	0.70
Co	---	0.19	---
Ni	0.0013	9.30	---
Cu	99.9905	0.16	0.30
Zn	0.0001	---	0.25
As	0.0003	---	---
Mo	---	0.17	---
Ag	0.0025	---	---
Cd	0.0001	---	---
Sn	0.0003	---	---
Sb	0.0008	---	---
Te	0.0002	---	---
Pb	0.0008	---	---

Table A.1. (continued)

Element (wt.%)	Graphite H-451 ρ = 1.74 g/cm^3	Boral[21] ρ = 2.53 g/cm^3	Plastic ρ = 0.95 g/cm^3	Lithium ρ = 0.534 g/cm^3
H	---	---	8.16	---
Li	---	---	---	100
B	---	15.7	---	---
C	100	4.3	48.64	---
O	---	---	43.20	---
Al	---	80.0	---	---

Table A.2. Graphite[22] H-451 Trace Elements

Element (wppm)	Impurity Contents
B	2
Na	10
Mg	1
Al	4
Si	21
S	1
Ca	22
Ti	1
V	1
Fe	3
Pb	7

Table A.3. Elemental Trace[23] Impurities

Trace Element (wppm)	Aluminum First Wall and Boral Material Element Fe	Cr	Mn
Nb	1	---	---
Mo	3	0.4	0.4
Ni	60	3	---
K	4	1	4
Cu	10	---	0.9
Ba	2	---	---

References

1. D.L. Henderson, R.R. Peterson and G.A. Moses, "Radioactivity in the Light Ion Fusion Target Development Facility," Fusion Tech. 8, 1396 (1985).

2. D.L. Henderson, G.A. Moses and R.R. Peterson, "Activation Studies of the Light Ion Beam Target Development Facility," submitted for publication in the Journal of Nuclear Materials.

3. R. Bangerter and D. Meeker, "Ion Beam Inertial Fusion Target Designs," UCRL-78474, Lawrence Livermore National Laboratory (1976).

4. M. Sawan et al., "Nuclear Analysis of the Heavy-Ion-Beam-Driven Fusion Reactor HIBALL," Nuclear Technology/Fusion 4, 79 (1983).

5. K. Long and N. Tahir, "Energy Deposition of Ions in Materials, and Numerical Simulations of Compression, Ignition, and Burn of Ion Beam Driven Inertial Confinement Fusion Pellets," KfK-3232, Kernforschungszentrum Karlsruhe (Oct. 1981).

6. "ANISN-ORNL," RSIC Code Package CCC-254, Radiation Shielding Information Center, Oak Ridge National Laboratory (1979).

7. "VITAMIN-C, 171 Neutron, 36 Gamma-Ray Group Cross Sections Library in AMPX Interface Format for Fusion Neutronics Studies," DLC-41, RSIC Data Library, Oak Ridge National Laboratory (1979).

8. "MACKLIB-IV, 171 Neutron, 36 Gamma-Ray Group Kerma Factor Library," DLC-60, RSIC Data Library, Oak Ridge National Laboratory (1979).

9. R.D. O'Dell et al., "User's Manual for ONEDANT: A Code Package for One-Dimensional, Diffusion-Accelerated, Neutral-Particle Transport," LA-9184-M, Los Alamos National Laboratory (Feb. 1982).

10. R. MacFarlane, "Nuclear Data Libraries from Los Alamos for Fusion Neutronics Calculations," Trans. Am. Nucl. Soc. 46, 271 (1984).

11. D. Garber, "ENDF/B-V," BNL-17541 (ENDF-201), National Nuclear Data Center, Brookhaven National Laboratory (Oct. 1975).

12. R. MacFarlane et al., "The NJOY Nuclear Data Processing System," Vols. I and II (ENDF-9203-M), Vol. I (LA-9303-M), Vol. II (ENDF-324), Los Alamos National Laboratory.

13. R. Alcouffe et al., "User's Guide for TWODANT: A Code Package for Two-Dimensional, Diffusion-Accelerated, Neutral-Particle Transport," LA-10049-M, Los Alamos National Laboratory (March 1984).

14. R.A. Lille, R.T. Santoro, R.G. Alsmiller, Jr., and J.M. Barns, "Neutron and Gamma Ray Streaming Calculations for the Engineering Test Facility Neutral Beam Injectors," Nucl. Tech./Fusion 2, 325-333 (1982).

15. D.L. Henderson, "DKR-ICF: A Radioactivity and Dose Rate Calculation Code Package," University of Wisconsin Fusion Technology Institute Report UWFDM-714 (November 1986).

16. M.A. Gordinier and R.J. Howerton, "ACTL: Evaluated Neutron, Activation Cross Section Library - Evaluation Techniques and Reaction Index," UCRL-50400, Vol. 18 (1978).

17. C.M. Lederer et al., Table of Isotopes, Sixth and Seventh Editions, Wiley (1967 and 1978).

18. American National Standard Neutron and Gamma-Ray Flux-to-Dose Rate Factors, ANSI/ANS-6.1.1-1977 (N666), published by the American Nuclear Society, 555 North Kensington Avenue, LaGrange Park, IL 60525.

19. Steven John Zinkle, "Effects of Thermal Annealing and Ion Irradiation on the Properties and Microstructures of Copper Alloys," Ph.D. Thesis, University of Wisconsin Fusion Technology Institute Report UWFDM-642 (May 1985).

20. D.W. Dorn and R.C. Maninger, "Issues in Radioactivity for Fusion Energy Remote Maintenance Rating," UCRL-89195, September 1983.

21. Theodore Rockwell, III, Reactor Shielding Design Manual, D. Van Nostrand Company (1965), p. 189.

22. G.R. Hopkins, R.J. Price, R.E. Bullick, J.A. Dalessandro and N.B. Elsner, "Carbon and Silicon Carbide as First Wall Materials in Inertial Confinement Fusion Reactors," GA-A14894 (March 1978).

23. HEDL Reduced Activation Program (material presented at the Planning Meeting for Development of Low Activation Austenitic and Ferritic Steels, ORNL, Feb. 7-8, 1984).